

Chemical abundances in M31 from H II regions

A. Zurita^{1,2*} and F. Bresolin^{3*†}

¹*Dpto. de Física y del Cosmos, Campus de Fuentenueva, Edificio Mecnas, Universidad de Granada, 18071–Granada, Spain*

²*Instituto Carlos I de Física Teórica y Computacional, Facultad de Ciencias, 18071–Granada, Spain*

³*Institute for Astronomy, 2680 Woodlawn Drive, Honolulu, HI 96822, USA*

ABSTRACT

We have obtained multi–slit spectroscopic observations from 3700 Å to 9200 Å with LRIS at the Keck I telescope for 31 H II regions in the disk of the Andromeda galaxy (M31), spanning a range in galactocentric distance from 3.9 kpc to 16.1 kpc. In 9 H II regions we measure one or several auroral lines ([O III]λ4363, [N II]λ5755, [S III]λ6312, [O II]λ7325), from which we determine the electron temperature (T_e) of the gas and derive chemical abundances using the *direct T_e -based method*. We analyze, for the first time in M31, abundance trends with galactocentric radius from the *direct* method, and find that the Ne/O, Ar/O, N/O and S/O abundance ratios are consistent with a constant value across the M31 disc, while the O/H abundance ratio shows a weak gradient. We have combined our data with all spectroscopic observations of H II regions in M31 available in the literature, yielding a sample of 85 H II regions spanning distances from 3.9 kpc to 24.7 kpc (0.19–1.2 R_{25}) from the galaxy center. We have tested a number of empirical calibrations of strong emission line ratios. We find that the slope of the oxygen abundance gradient in M31 is -0.023 ± 0.002 dex kpc⁻¹, and that the central oxygen abundance is in the range $12+\log(\text{O}/\text{H}) = 8.71\text{--}8.91$ dex (i.e. between 1.05 and 1.66 times the solar value, for $12+\log(\text{O}/\text{H})_{\odot} = 8.69$), depending on the calibration adopted. The H II region oxygen abundances are compared with the results from other metallicity indicators (supergiant stars and planetary nebulae). The comparison shows that H II region O/H abundances are systematically ~ 0.3 dex below the stellar ones. This discrepancy is discussed in terms of oxygen depletion onto dust grains and possible biases affecting T_e -based oxygen abundances at high metallicity.

Key words: galaxies: abundances – (*galaxies*): Local Group – galaxies: ISM – galaxies: individual: M31 – (*ISM*): H II regions – ISM: abundances

1 INTRODUCTION

M31, the Andromeda galaxy, is our nearest neighbour and the largest galaxy of the Local Group and these properties make this galaxy a fundamental benchmark for understanding spirals and their evolution. M31’s proximity allows for spatially detailed studies of its constituent stellar populations, even though the large angular extent on the sky hampers a global view of this galaxy. The advent of large field cameras and multi-object spectrographs has been critical for a growing amount of information on important properties of M31. These improvements in observational capabilities have permitted, for example, the discovery of a giant stellar tidal stream in the halo (Ibata et al. 2001) and detailed studies of the resolved stellar populations both in the disc and in the halo (e.g. Ferguson et al. 2002, 2005;

Davidge et al. 2012; Tanaka et al. 2010) which have radically changed our knowledge on the formation and evolution of M31. It is now recognized that interactions and satellite accretions have been widely responsible for the evolution of the Andromeda galaxy (e.g. Ibata et al. 2001; Bernard et al. 2012; Davidge et al. 2012; Hammer et al. 2007). The interstellar medium also shows signatures of disruptions possibly resulting through these interactions (e.g. Unwin 1983; Corbelli et al. 2010). The current star formation rate (SFR) across the disc, $\sim 1 M_{\odot} \text{ yr}^{-1}$ (Williams 2003), is significantly lower than in the Milky Way and most of the star-forming sites are distributed in a prominent ring of approximately ~ 10 kpc galactocentric radius. This morphology has been predicted with dynamical models of the recent interaction of M31 with a companion galaxy (possibly M32, Block et al. 2006).

The chemical evolution of M31 has also been extensively studied in comparison with the Milky Way (Marcon-Uchida, Matteucci, & Costa 2010; Yin et al. 2009;

* E-mail: azurita@ugr.es

† E-mail: bresolin@ifa.hawaii.edu

Renda et al. 2005). Both Local Group galaxies seem to share common features in their chemical evolution, but in order to explain the observations in detail, models require different formation histories for the two galaxies. In particular, M31 must have been more active and efficient in the past in forming stars than the Milky Way (Yin et al. 2009; Renda et al. 2005).

The present-day chemical element abundances and their spatial distribution across a galaxy are key observational properties for constraining different models of chemical evolution (e.g. Marcon-Uchida et al. 2010). H II regions have been traditionally the main targets used to trace the present-day elemental abundances across galaxy disks. However, nebular metallicity data on M31 are surprisingly sparse. Since the first H II region emission-line strength measurements made by Rubin, Krishna Kumar, & Ford (1972) in the early 1970's, in which the existence of an abundance gradient was suggested, only a handful of authors have tried to measure the abundance gradient of M31. Dennefeld & Kunth (1981) analyze a sample of 12 supernova remnants (SNR) and 8 H II regions. They report gradients in the N/H and N/O ratios across the galaxy disk, but no gradient in the distribution of oxygen abundance with galactocentric radius, within the large uncertainties in their abundances determinations. In a subsequent study, Blair, Kirshner, & Chevalier (1982) obtain an oxygen abundance gradient with a slope of approximately -0.027 dex kpc^{-1} and a super-solar oxygen abundance in the M31 center ($12+\log(\text{O}/\text{H}) > 9.0$) from the application of empirical *strong-line* nebular metallicity determination methods to the observed line fluxes in a sample of 11 H II regions. In the same paper they calculate the oxygen abundance gradient from the spectra of 9 SNRs, and these show no significant gradient across the disk, with a mean abundance $12+\log(\text{O}/\text{H}) \simeq 8.5$. The most recent spectroscopic observations of a sample of H II regions in M31 date from the late 1990's and were presented by Galarza, Walterbos, & Braun (1999) and Bresolin, Kennicutt, & Garnett (1999). The former use the R23 parameter and find a somewhat steeper oxygen gradient, with a slope of -0.06 ± 0.03 dex kpc^{-1} . All these authors derive the chemical abundance gradient in M31 by applying empirical calibrations of bright-line ratios, as the temperature sensitive auroral lines used to constrain electron temperature and emissivities of abundance-sensitive forbidden lines (i.e. through the *direct method*) remained undetected. In fact, it is somewhat surprising that, to-date, there are no auroral line detections for the determination of H II region abundances through the *direct method* in M31, apart from a single H II region (K932) observed by Esteban et al. (2009).

Other attempts to measure the oxygen abundance gradient in M31 come from the reanalysis of the datasets mentioned above (mainly those of the 1980's) and the application of different *strong-line methods* (Zaritsky, Kennicutt, & Huchra 1994; Vila-Costas & Edmunds 1992; Smartt et al. 2001; Trundle et al. 2002). The M31 oxygen abundance gradient slope derived by the different authors ranges from -0.013 dex kpc^{-1} to -0.06 dex kpc^{-1} , i.e. they differ by as much as a factor of four, mainly due to uncertainties and differences in the strong-line methods used. The central

Table 1. Journal of observations.

Mask	$\Delta\lambda$ (Å, FWHM)	Spectral range ^a (Å)	Exposure Time (s)
1	5.6	3450–6000	$3 \times 1800 + 2 \times 1200$
1	4.5	5120–6840	3×1800
1	9.3	6450–10000	2×1200
2	5.6	3450–6000	$3 \times 1800 + 2 \times 1000$
2	4.5	5120–6840	3×1800
2	9.3	6450–10000	2×1000
3	5.6	3450–6000	$2 \times 1800 + 2 \times 1000$
3	4.5	5120–6840	2×1800
3	9.3	6450–10000	2×1000

^a Approximate spectral range for a slit in the centre of the detector.

oxygen abundance that results from these studies ranges between 1 and 3.5 times the solar value.

Motivated by the desirability of a modern re-evaluation of the present-day chemical abundance in M31, we secured new spectra of H II regions in the Andromeda galaxy, in order to obtain nebular chemical abundances based on the detection of the faint auroral lines used for electron temperature determinations. The main aim of the current paper is to measure the oxygen abundance gradient from H II regions in M31 and to compare with other metallicity indicators, in particular young, massive stars (Venn et al. 2000; Trundle et al. 2002; Smartt et al. 2001) and planetary nebulae (Kwitter et al. 2012).

This paper is organized as follows. The spectroscopic observations, the data reduction procedure and the methodology employed for measuring emission line fluxes are described in Sec. 2. In Sec. 3 we derive the physical properties (electron densities and temperatures) of the H II regions and from these, the ionic and total chemical abundances are obtained (Sec. 4). The radial oxygen abundance gradient is then calculated (Sec. 5) from our *direct measurements* and from empirical metallicity calibrations applied to the H II regions of our sample and to a compilation of data from other authors. A comparison with other metallicity indicators is presented in Sec. 6. Finally, in Sec. 7 we discuss and summarize our results.

2 OBSERVATIONS AND DATA REDUCTION

2.1 Observations

The spectroscopic observations of H II regions in the disk of M31 were carried out on 2005 September 29 with the Low Resolution Imaging Spectrometer (LRIS, Oke et al. 1995) at the 10m Keck I telescope operated by the W.M. Keck Observatory on the Mauna Kea summit. The sky was photometric with seeing $\sim 0.8''$ at the beginning of the night. Conditions slowly got worse, having seeing $\sim 1.5''$ at the end of the night.

LRIS was used in multi-slit mode. Both the blue and red channels of the spectrograph were used simultaneously with a dichroic beam splitter (with 50% transmittance at 5091 Å) for two different setups. The first setup was used to cover the spectral range 3500 Å to 6840 Å for a slit at the center of the detector with spectral resolution and dispersion ~ 5.6 Å (FWHM) and 0.62 Å/pix, respectively, in the blue

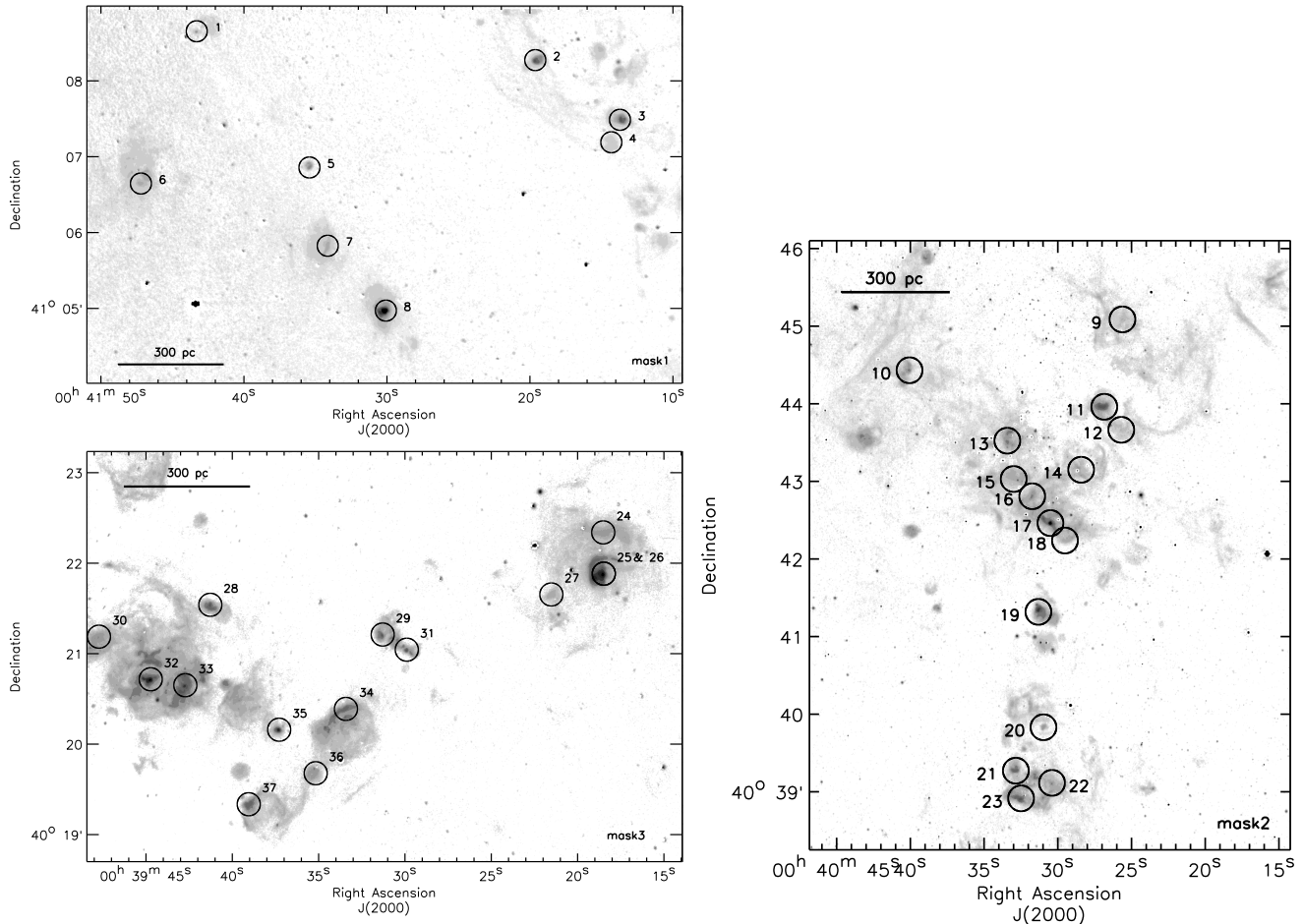


Figure 1. Identification of the targets included in our LRIS Keck multi-slit masks plotted over an H α continuum-subtracted image obtained at the 2.5m Isaac Newton Telescope at la Palma. The circles mark the brightest H α knots along each slit, where the apertures for the one dimensional spectrum extractions were centred.

Table 2. M31 adopted parameters.

Parameter	Value	References
RA (J2000)	00h 42m 44.33s	Skrutskie et al. (2006)
Dec (J2000)	+41°16' 07.50"	Skrutskie et al. (2006)
Inclination	77°	Corbelli et al. (2010)
Position angle	38°	Corbelli et al. (2010)
Distance	(744 ± 33) kpc	Vilardell et al. (2010)
R ₂₅ (arcmin)	(95 ± 2)	de Vaucouleurs et al. (1991)
R ₂₅ (kpc)	(21 ± 1)	

channel (with a 600 lines mm⁻¹ grism blazed at 4000 Å) and ~4.5 Å (FWHM) and 0.62 Å/pix in the red channel (with a 900 lines mm⁻¹ grating blazed at 5500 Å). The second setup was identical in the blue channel, but included a 400 lines mm⁻¹ grating blazed at 8500 Å in the red arm, covering roughly from 6450 Å to 10000 Å with 9.3 Å FWHM resolution. The blue channel spectra were imaged on a mosaic of two 2K×4K Marconi (E2V) CCDs giving a plate scale of 0.135'' pix⁻¹, the red channel spectra on a back-illuminated Tektronix 2K×2K CCD, with 0.215'' pix⁻¹.

Three slit masks were defined and used for the multi-object spectroscopy, centered approximately 17', 42' and 66' from the nucleus of M31. The masks cover 4.8'×7.3' on the sky, and contained 8, 15 and 13 1.2''-wide slits, respectively.

The slit lengths varied between 7'' and 1.5'. The observations were carried out ensuring that the slit position angle in each mask was within 20° of the parallactic angle for airmasses greater than 1.3, in order to minimize light losses due to differential atmospheric refraction. Table 1 contains a journal of the observations.

The target H II regions were selected from H α continuum-subtracted images (see Fig. 1), previously obtained with the Wide Field Camera of the 2.5m Isaac Newton Telescope (INT) at La Palma (Spain) within the Local Group Census project¹ (e.g. Magrini et al. 2002). An astrometric calibration of these images with an accuracy of 0.3 arcsec was secured using stellar positions from the USNO2 (Monet 1998) catalogue. The positions of the selected H II regions across the M31 disc are shown in Fig. 2 and their coordinates are given in Table 3. Four targets are in common with the Blair et al. (1982) sample (BA423, BA379, BA416, BA370; the last two were classified as SNRs by these authors).

¹ The Local Group Census is a narrow-band imaging survey of all the galaxies of the Local Group above Dec = -30° (<http://www.ing.iac.es/~rcorradi/LGC/>).

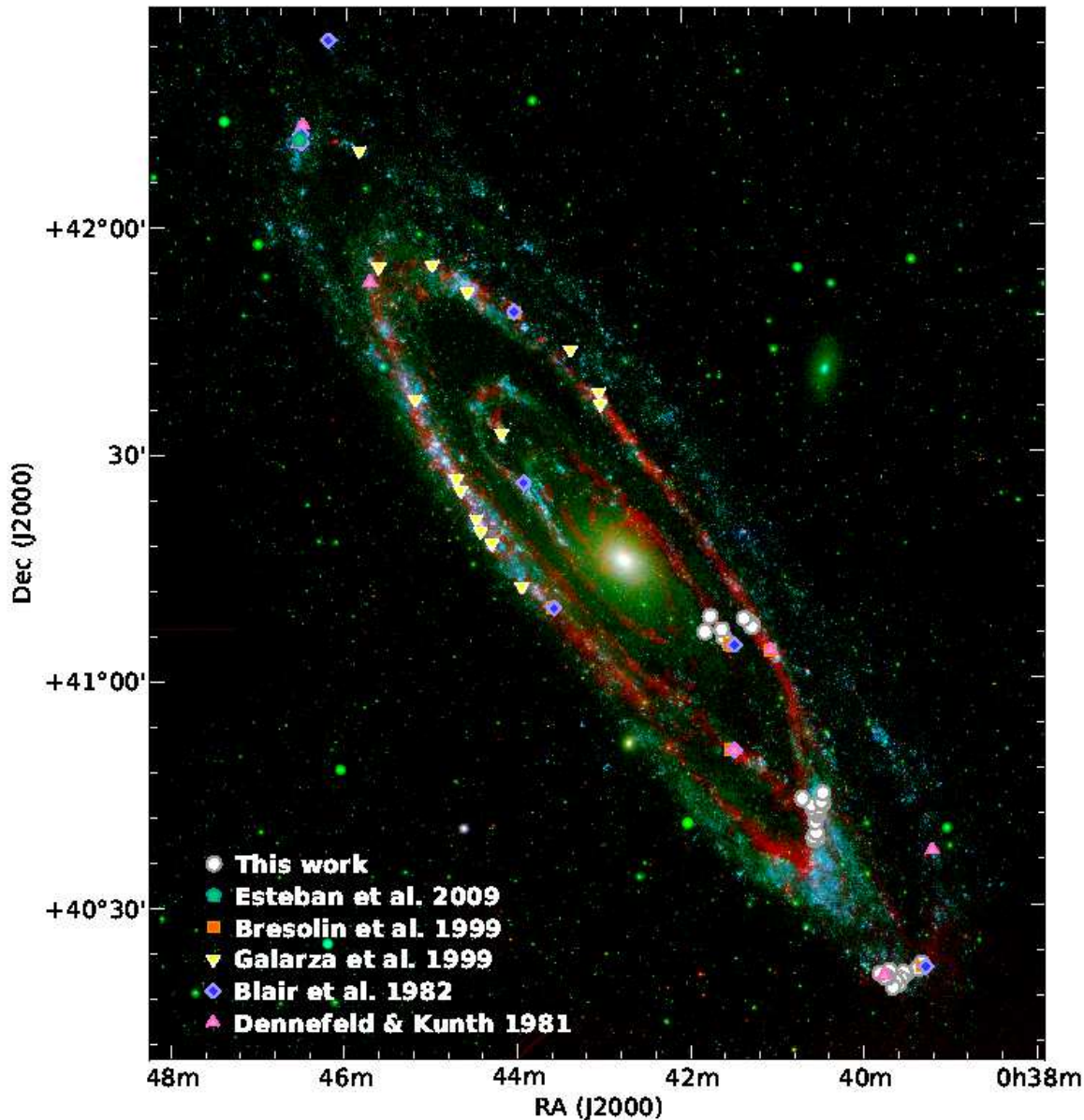


Figure 2. Image of M31 showing the location of the H II studied in this work (white circles). H II regions studied by other authors are indicated with pink triangles (Dennefeld & Kunth 1981), violet diamonds (Blair et al. 1982), yellow squares (showing slit centers by Galarza et al. 1999), inverted orange triangles (Bresolin et al. 1999) and cyan pentagon (Esteban et al. 2009). The image is a composite of GALEX (FUV: blue, NUV: green) and Spitzer ($24 \mu\text{m}$: red).

2.2 Data reduction

The data reduction was carried out using standard IRAF² techniques. After removing the bias level, a correction was applied to account for the different gains (e^-/ADU) of the amplifiers of the red and blue CCDs. Afterwards the spectrum corresponding to each slit was identified and separated out from the 2-dimensional slit mask spectra of science and calibration frames, and in subsequent tasks the

spectrum from each slit was treated as a separate spectrum. The data reduction was then carried out using standard procedures for long-slit spectra: flatfielding, cosmic-ray removal (`lacos_spec`, van Dokkum 2001), removal of geometrical distortions in the spectral and spatial directions, wavelength calibration, extraction of one dimensional spectra within defined apertures and combination of the individual spectra.

The final spectra were flux calibrated using observations of the spectrophotometric standards BD+28 4211, G191-B2B, Hiltner 600 and GD71 that were obtained at the beginning, middle and end of the night with a $8.7''$ -wide slit. The standard star fluxes have been obtained from Oke (1990), Bohlin, Colina, & Finley (1995), and Hamuy et al.

² IRAF is distributed by the National Optical Astronomy Observatories, which is operated by the Association of Universities for Research in Astronomy, Inc. (AURA) under cooperative agreement with the National Science Foundation.

Table 3. H II region equatorial coordinates and galactocentric distances.

ID ^a	RA	Dec	Galactocentric distance ^b	Other ID ^c
	(J2000)		(kpc)	
1	00:41:43.67	+41:08:40.27	5.05	–
2 [†]	00:41:19.94	+41:08:21.38	8.16	BA 419, P 318
3 [†]	00:41:13.96	+41:07:35.09	8.64	BA 422, P 310
4	00:41:14.54	+41:07:17.25	8.42	P 308
5 ^{†,‡}	00:41:35.65	+41:06:53.86	5.42	BA 416 (SNR candidate), P 325*
6	00:41:47.42	+41:06:39.13	3.93	BA 415 (SNR candidate), P 327
7	00:41:34.30	+41:05:52.14	5.23	P 317
8 ^{†,‡}	00:41:30.17	+41:05:01.51	5.47	BA 423, P 309*
9	00:40:26.10	+40:45:08.45	8.85	P 182
10	00:40:40.52	+40:44:26.75	8.58	–
11	00:40:27.26	+40:44:00.71	8.93	BA 464, P 176
12	00:40:26.08	+40:43:43.06	9.01	P 173
13	00:40:33.81	+40:43:33.39	8.86	P 179
14 [‡]	00:40:28.77	+40:43:11.74	9.02	P 171
15	00:40:33.35	+40:43:03.86	8.97	P 174?
16	00:40:32.07	+40:42:50.72	9.04	P 174?
17 [†]	00:40:30.81	+40:42:30.19	9.13	BA 310, P 167
18	00:40:29.81	+40:42:16.84	9.19	–
19 [†]	00:40:31.55	+40:41:21.40	9.41	BA 312, P 161
20	00:40:31.11	+40:39:52.24	9.85	–
21	00:40:32.94	+40:39:18.35	10.07	BA 318, P 150
22 [‡]	00:40:30.48	+40:39:09.33	10.07	P 145
23	00:40:32.57	+40:38:57.02	10.18	BA 319, P 149
24	00:39:18.84	+40:22:26.04	14.53	BA 375, P 15
25 [†]	00:39:18.77	+40:21:58.66	14.66	BA 379, P 7*
26 [†]	00:39:18.77	+40:21:58.66	14.66	BA 379, P 7*
27	00:39:21.79	+40:21:44.31	14.74	BA 378, P 9
28	00:39:41.55	+40:21:33.54	15.25	BA 358, P 32
29 ^{†,‡}	00:39:31.53	+40:21:15.81	15.06	BA 368, P 21
30	00:39:47.97	+40:21:11.07	15.67	BA 357, P 34
31	00:39:30.12	+40:21:06.05	15.09	BA 373
32 ^{†,‡}	00:39:44.93	+40:20:43.43	15.73	BA 360
33 [†]	00:39:42.92	+40:20:39.90	15.67	BA 362
34 [†]	00:39:33.59	+40:20:26.06	15.42	BA 374, P 17
35 [†]	00:39:37.44	+40:20:11.49	15.65	BA 371, P 20
36	00:39:35.28	+40:19:43.06	15.76	BA 377, P 11
37	00:39:39.13	+40:19:21.71	16.06	BA 376, P 14

^a Nebulae with auroral line detections are indicated with †. A double dagger (‡) indicates supernova remnant candidates.

^b Galactocentric distances computed from the M31 orientation parameters shown in Table 2.

^c IDs starting with *BA* from Baade & Arp (1964) and with *P* from Pellet et al. (1978). Nebulae marked with * have been spectroscopically observed by Blair et al. (1982).

(1994). A standard mean optical/near-IR extinction curve for Mauna Kea was adopted for the atmospheric extinction correction (from the UKIRT web pages³).

Given the limited near-IR range of most of the spectrophotometric standard star spectra, only data below 9200 Å are useful. The [S III]λ9532 fluxes have been calculated from the theoretical ratio [S III]λ9532/[S III]λ9069=2.44.

2.3 Emission line flux measurements and interstellar extinction correction

The emission line fluxes of the H II regions were measured with the `SPLIT` IRAF task, by integrating all the flux in the emission line between two given limits over the local continuum level defined interactively.

We analysed the spectra of 37 nebulae. Two of them correspond to different extractions of the same slit, in which two bright knots of ionized gas emission (objects 25 and 26 in Table 3) were identified. For 13 targets we were able to detect one or several of the following auroral lines, [O III]λ4363, [N II]λ5755, [S III]λ6312, and [O II]λ7325, which allow the determination of the electron temperature of the different ions, although four of the targets turned out to be SNR, as described below. The other 24 targets have lower signal-to-noise spectra and no auroral lines were detected. We identified two SNR candidates within this subsample. For the

³ <http://www.jach.hawaii.edu/UKIRT/astronomy/utls/exts.html>. This extinction curve comes from CFHT Bulletin (Bèland, Boulade, & Davidge 1988) and the CFHT observer’s manual.

remaining 22 H II regions we concentrate here only on the brightest emission lines, which will be used for the determination of the oxygen abundances through *strong-line methods* (Sect. 5.1).

The three different spectral ranges (blue, red and near-infrared) were scaled in order to bring them to the same relative flux calibration. Several emission lines in common between the red and the near-infrared spectral ranges (typically H α , [N II] $\lambda\lambda$ 6548, 6583, He I λ 6678, [S II] $\lambda\lambda$ 6717, 6731) provided the scaling factor. There are no lines in common between the blue and the red spectral ranges. In this case a preliminary scaling factor was obtained from the continuum level of both spectra. The final scaling factor was later determined by imposing the expected H α /H β flux ratio (Storey & Hummer 1995) for the measured or assumed electron temperature, after the interstellar extinction and stellar absorption corrections had been applied (see below).

The interstellar reddening was determined from the Balmer series hydrogen recombination lines flux decrement. As the fluxes of nebular Balmer emission lines are affected by absorption by the underlying stellar population, a correction needs to be applied in order to obtain the interstellar extinction to properly correct our measurements. We have assumed that the equivalent width of the stellar absorption (EW_{abs}) is the same for all Balmer lines. Then, an iterative procedure was performed: the extinction coefficient $c(H\beta)$ was determined from the comparison of the measured fluxes of the H γ and H δ lines relative to H β and the expected ratios from the case B recombination given by Storey & Hummer (1995) for an electron temperature of 7500 K and density of 100 cm^{-3} . The Howarth (1983) parametrization of the interstellar reddening law by Seaton (1979) was adopted for $R_V=3.1$. The EW_{abs} was then adjusted in successive iterations until the $c(H\beta)$ value obtained from the H γ /H β and H δ /H β line ratios were in agreement. After the determination of the electron temperature (see Sect. 3) the iterative process was repeated. We checked that higher order recombination lines of the Balmer series measured in our spectra were in agreement (within errors) with the theoretical predictions. The extinction coefficient $c(H\beta)$ obtained varies between 0.24 and 1.0 in our H II region sample, while the EW_{abs} was found to be in the range 1.5–3.2 Å for the highest S/N spectra, where we detected the auroral lines. For the lowest S/N spectra, the extinction coefficient $c(H\beta)$ was typically determined from the H γ /H β ratio alone (and in this case the EW_{abs} was assumed to be zero) or from both H γ /H β and H δ /H β when possible. $c(H\beta)$ for these regions ranges from 0.0 to 1.03.

The final values of $c(H\beta)$, EW_{abs} , and the blue–red scaling factor were further checked in the highest S/N H II region spectra by comparing the observed He I line ratios with theoretical predictions (Benjamin, Skillman, & Smits 1999). The observed and theoretical He I line ratios λ 5876/ λ 4471, λ 6678/ λ 4471 and λ 5876/ λ 4922 differ by less than 15% in all targets, except for #5, for which differences are larger (of order \sim 40%). We note that the observational errors for these ratios are also higher (\sim 30%) for this target, which turned out to be a SNR (see Sect. 2.4). The same check was done with the Balmer ratio H ϵ /H β and Paschen series line ratios to H β when available (using mainly Pa 9, Pa 10, Pa 11, Pa 12). In this case the observed and theoretical line ratios differ by less than 20% (typically \sim 5–10%), except for the H ϵ /H β

ratio in targets #5, #25, #26 and #35 for which the difference observed–theoretical is larger, \sim 25–30%, except for target #5 (SNR) in which H ϵ is twice the value expected for an H II region possibly due to blending with enhanced [Ne III] (Stupar, Parker, & Filipović 2008).

Table 4 shows the line fluxes corrected for reddening and normalized to H β for the 13 nebulae where auroral lines fluxes have been measured. For the remaining targets (with no detections of auroral lines) we give in Table 5 the brightest line fluxes corrected for reddening and normalized to H β . The coordinates and galactocentric distances for both sets of regions are given in Table 3.

The uncertainties quoted in Tables 4 and 5 include (added in quadrature): statistical errors measured with SPLIT, flatfielding errors, the uncertainty in the flux calibration, and the uncertainty in the determination of the flux scaling factors between the different spectral ranges and in the determination of the extinction coefficient. Typically, errors in the line flux ratios are of order \sim 4–8% for lines brighter than $F_{H\beta}/2$, and \sim 6–16% for fainter lines, for the H II regions with detections of auroral lines. For the regions with lower S/N the errors in the line flux ratios relevant for *strong-line methods* for abundance determinations are of order \sim 5–20% for [O II]/H β , \sim 5–40% for [O III] λ 4959/H β , \sim 4–30% for [O III] λ 5007/H β , and \sim 5–20% for [N II] λ 6583/H β .

Four of our targets are located within \sim 3" of the positions reported by Blair et al. (1982, see Table 3). We have compared the fluxes published by these authors with the fluxes of our brightest lines. The measurements agree within 15% for lines brighter than $F_{H\beta}/3$ across the whole spectral range in common (from 3700 Å to 6730 Å). The differences are higher for [S II] $\lambda\lambda$ 6717, 6731 in #5 (BA416), \sim 35%, and for [O II] λ 3727 in #25 (BA379), \sim 50%. For line ratios fainter than $F_{H\beta}/3$ the differences increase up to \sim 60% (in both directions), with no dependence on wavelength. We note that Blair et al. (1982) state that their error in faint line fluxes ($< 0.5 F_{H\beta}$) may be as large as 50%.

2.4 Supernova remnants

Targets #5 (BA416) and #29 (BA370) are classified as SNRs by Blair et al. (1982). For both nebulae we find [S II]/H $\alpha > 0.5$, indicating the presence of shocks. Our measured line ratios for BA416 position this region in the area of the H α /[S II] vs. H α /[N II] diagnostic diagram that corresponds to SNR (Sabbadin, Minello, & Bianchini 1977), in agreement with the conclusion by Blair et al. (1982). According to our measurements, the location of BA370 in the same diagnostic diagram does not allow us to clearly establish the nature of this nebula. However, we measure a substantial [O I] $\lambda\lambda$ 6300, 6360 flux ([O I]/H $\beta > 0.4$). Following the line ratio diagnostic criteria of Fesen, Blair, & Kirshner (1985) ([O II]/H β vs. [O I]/H β) both BA416 and BA370 are identified as SNRs. We note that, as mentioned above, Blair et al. (1982) reported a \sim 35% higher [S II] $\lambda\lambda$ 6717, 6731 flux for BA416 than determined from our observations. Given that the center position of our slit does not perfectly coincide with theirs, we cannot exclude some dilution of the SNR emission by surrounding photoionized gas emission in our spectrum.

Table 4: Reddening-corrected line fluxes in nebulae with auroral line detections.

	λ_o (Å)	#2	#3	#5*	#8*	#17	#19	#25	#26	#29*	#35	#32*	# 33	#34
5+He I	3704	...	1.34±0.08	...	0.98±0.05	1.11±0.10	...	1.00±0.06	1.42±0.12
5	3712	...	1.35±0.08	...	0.85±0.04	1.48±0.13	...	1.07±0.07	0.96±0.08
]	3727	210±20	170±10	770±60	150±7	143±13	159±8	158±10	230±20	330±20	150±10	269±20	220±2	289±14
2	3750	1.94±0.14	2.39±0.14	...	1.69±0.08	1.9±0.2	...	1.87±0.12	2.9±0.2	...	3.1±0.2	1.73±0.10	1.57±0.11	...
1	3771	5.4±0.3	5.2±0.2	...	5.0±0.2	4.0±0.3	...	4.9±0.3	4.5±0.3	6.0±0.3	4.3±0.2	4.0±0.2	7.3±0.4	4.7±0.2
0	3798	7.0±0.4	6.0±0.3	4.1±0.3	6.0±0.2	5.3±0.4	7.0±0.3	5.8±0.3	5.8±0.5	7.3±0.4	5.1±0.3	5.3±0.3	6.6±0.4	7.5±0.3
	3819	0.52±0.02	0.69±0.06	1.19±0.10	...	0.90±0.06	0.73±0.04
	3835	9.0±0.5	8.5±0.4	10.4±0.8	8.0±0.3	6.9±0.6	8.5±0.3	7.8±0.4	7.9±0.6	8.0±0.4	7.0±0.4	7.2±0.4	8.0±0.5	7.0±0.3
III]	3868	2.2±0.2	...	77±6	0.71±0.03	4.4±0.4	...	14.7±0.9	13.2±1.1	...	18.7±1.2	3.8±0.2	...	5.8±0.3
	3889	15.3±1.1	14.9±0.9	18.3±1.4	13.0±0.6	16.2±1.4	13.7±0.7	16.4±1.0	19±2	15.7±0.9	17.6±1.1	15.1±0.8	12.4±0.9	17.0±0.8
	3969	16.4±1.1	15.1±0.8	32±2	12.4±0.5	16.4±1.3	14.1±0.6	19.8±1.2	20±2	15.1±0.8	21.1±1.3	16.2±0.8	15.7±1.0	16.0±0.7
	4026	0.78±0.05	0.85±0.04	1.62±0.13	...	1.05±0.06	1.68±0.14	...	2.04±0.12	1.09±0.06
	4072	1.75±0.12	...	18.4±1.3	2.90±0.14	1.2±0.1	1.94±0.09	0.94±0.06	1.30±0.11	4.9±0.3	1.00±0.06	3.5±0.2
	4101	25±2	25.5±1.4	27±2	25.3±1.1	25±2	25.5±1.1	25±2	26±2	25.5±1.4	25±2	25.3±1.3	25.5±2	25.9±1.2
	4144	0.47±0.04
I]	4244	0.20±0.01
	4267	0.22±0.01
I]	4287	0.23±0.01
	4340	46±3	47±3	44±3	46±2	47±3	46±2	47±3	47±4	47±3	47±3	47±2	47±3	47±2
I]	4363	22.1±1.4	0.34±0.02	0.40±0.03	...	1.30±0.08	1.20±0.10	...	1.35±0.08	0.97±0.05
	4388	0.27±0.01	0.41±0.03	...	0.23±0.01	0.61±0.05	...	0.81±0.05	0.33±0.02
I]	4414	3.7±0.2	0.36±0.02	0.53±0.03
	4471	2.9±0.2	3.4±0.2	2.19±0.13	2.82±0.13	3.8±0.3	2.23±0.11	3.6±0.2	4.2±0.3	2.41±0.14	4.3±0.3	3.2±0.2	2.2±0.2	4.3±0.2
I]	4563	0.24±0.01	0.15±0.01	0.37±0.02
I]	4571	0.16±0.01	0.15±0.01
II]	4658	4.6±0.3	0.89±0.04	0.99±0.05
I	4686	7.4±0.4	1.57±0.07
II]	4702	2.23±0.13	0.23±0.01	0.08±0.01	0.33±0.02
	4713	3.2±0.2	0.24±0.01	0.37±0.02	...	0.31±0.02	0.45±0.04	0.32±0.02
IV]	4740	1.36±0.08
II]	4755	2.02±0.12	0.16±0.01
	4861	100±7	100±6	100±6	100±5	100±7	100±5	100±6	100±8	100±6	100±6	100±5	100±7	100±5
II]	4881	1.35±0.08	0.27±0.01	0.25±0.01
	4922	0.77±0.05	0.91±0.05	0.70±0.04	0.80±0.04	1.04±0.07	...	0.91±0.05	1.17±0.09	...	1.22±0.07	0.76±0.04
I]	4959	22±2	15.6±0.9	122±7	8.9±0.4	40±3	11.7±0.6	86±5	75±6	12±0.7	104±6	36±2	20.5±1.4	59±2
II]	4986	5.1±0.3	0.57±0.03	0.16±0.01	0.24±0.02	1.26±0.06
I]	5007	58±4	44±2	350±20	27±1	114±8	34±2	251±14	220±20	34±2	320±20	102±5	59±4	180±9
	5016	1.62±0.11	1.82±0.10	...	1.69±0.08	2.2±0.2	1.49±0.07	2.09±0.12	2.2±0.2	...	2.8±0.2	1.84±0.09	1.51±0.10	2.03±0.10
I]	5159	3.4±1.1
	5199	...	0.75±0.08	18±2	3.4±0.2	0.43±0.07	0.9±0.2	0.56±0.05	0.91±0.08	8.5±0.6	0.57±0.14	1.3±0.2
I]	5262	1.7±1.0	0.11±0.03

Chemical abundances in M31 from H II regions

Table 4: Continued.

	λ_o (Å)	#2	#3	#5*	#8*	#17	#19	#25	#26	#29*	#35	#32*	# 33	#34
[II]	5270	5±2	0.46±0.03	0.56±0.04
[II]	5518	0.25±0.05	0.30±0.04	...	0.27±0.02	0.35±0.05	...	0.46±0.04	0.39±0.05	...	0.40±0.09	0.33±0.03
[II]	5538	0.19±0.04	0.20±0.04	...	0.23±0.02	0.24±0.04	...	0.30±0.03	0.29±0.05	...	0.25±0.07	0.24±0.03
[I]	5755	0.50±0.08	0.69±0.06	6.1±1.1	0.86±0.05	0.43±0.06	0.51±0.10	0.40±0.03	0.66±0.06	1.3±0.2	0.45±0.08	0.78±0.05	0.70±0.07	1.6±0.2
[I]	5876	9.8±1.0	10.5±0.6	10.6±1.3	9.2±0.4	12.9±1.0	9.4±0.5	11.6±0.7	11.8±0.8	7.1±0.5	11.4±0.9	9.1±0.5	7.2±0.4	11.7±0.6
[I]	5959	0.09±0.02
[I]	5978	0.13±0.02	0.11±0.02
[I]	6300	1.24±0.14	...	73±6	5.6±0.3	0.88±0.09	1.40±0.14	1.12±0.07	1.77±0.13	27±2	0.94±0.10	6.0±0.4	1.60±0.12	5.6±0.3
[I]	6312	0.60±0.07	...	2.6±0.8	0.60±0.04	0.97±0.11	...	1.21±0.08	1.37±0.10	...	1.45±0.14
[I]	6347	0.25±0.03
[I]	6360	0.39±0.06	...	23±2	2.11±0.11	0.27±0.04	...	0.28±0.03	0.59±0.05	9.8±0.6	...	2.01±0.13	0.38±0.05	1.7±0.2
[I]	6548	26±3	26.7±2	121±11	44±2	20±2	32±2	10.7±0.7	16.3±1.1	33±2	11.0±0.9	21.1±1.3	24±2	32±2
[I]	6563	290±30	300±20	300±30	293±20	289±3	300±20	290±20	280±20	294±20	300±30	280±20	290±20	284±14
[I]	6583	81±8	80±4	370±30	133±7	63±6	97±5	32±2	48±3	101±6	34±3	64±4	71±5	98±5
[I]	6678	2.9±0.3	3.2±0.2	3.2±0.9	2.59±0.13	3.5±0.3	2.7±0.2	3.3±0.2	3.4±0.3	2.3±0.2	3.4±0.3	2.6±0.2	2.2±0.2	2.9±0.2
[I]	6717	23±2	22.5±1.2	160±20	44±2	15±2	29±2	10.9±0.7	17.7±1.3	94±6	12.7±1.1	39±3	28±2	42±2
[I]	6731	17±2	16.5±0.9	131±13	36±2	11.0±1.1	20.1±1.1	7.9±0.6	12.4±0.9	70±5	9.2±0.8	29±2	19.7±1.3	29±2
[I]	7065	1.3±0.2	1.39±0.11	...	1.19±0.07	1.9±0.2	1.3±0.3	2.0±0.8	1.9±0.2	2.1±0.6	2.0±0.2	1.3±0.8	1.5±0.2	1.6±0.3
[I]	7135	6.1±0.7	6.0±0.4	10±4	4.6±0.2	8.9±1.0	5.5±0.5	9.8±0.9	9.7±0.7	3.1±0.5	10.8±1.0	6.1±1.0	5.4±0.4	11.7±0.7
[I]	7236	2.2±0.5	...	0.35±0.06
[I]	7281	0.5±0.2	0.68±0.09
[I]	7325	2.0±0.3	...	37±5	3.0±0.2	2.4±0.3	...	3.2±0.8	5.0±0.4	6.1±1.1	6.2±0.5	8.9±0.6
[I]	7378	8.6±1.1
[I]	7751	1.3±0.2	1.04±0.06	2.2±0.3	...	2.3±0.5	2.2±0.2	...	2.5±0.4	1.5±0.7
[I]	8502	0.7±0.2
[I]	8545	1.0±0.2
[I]	8598	1.3±0.2
[I]	8665	3.7±0.5
[I]	8750	1.1±0.2	1.21±0.06	0.94±0.14
[I]	8863	1.4±0.2	1.43±0.07
[I]	9015	1.7±0.3	1.60±0.08	2.1±0.3
[I]	9069	23±3	20.8±1.3	11±2	19±1	23±3	19.3±1.3	21±2	22±2	8.00±2	21±2	16±2	20±3	13.4±1.2
[I]	9229	2.5±0.4	2.43±0.13	2.9±0.4	...	2.4±0.2	2.0±0.2	...	2.3±0.4	2.0±0.8	2±2	...
[I]		0.21±0.04	0.31±0.02	0.76±0.1	0.67±0.02	0.55±0.10	0.44±0.02	0.43±0.05	0.42±0.04	0.34±0.04	1.00±0.05	0.39±0.05	0.54±0.04	0.44±0.02
[I]		189.6±0.4	198.7±0.4	166.6±1.1	156.90±0.14	226.1±0.4	74.9±0.3	123.4±0.1	377.6±0.6	174.1±0.8	908±2	186.0±0.2	82.3±0.2	184.0±0.5
[I]		11.1±0.5	13.0±0.5	3.9±0.2	142±5	21±1	9.8±0.3	53±2	25.5±1.4	3.5±0.1	26±1	35.7±1.2	17.3±0.8	9.4±0.3

indicates SNRs candidates (see Sect. 2.3) for details.

$\gamma(\text{H}\beta)$ is the total extinction-corrected $\text{H}\beta$ flux in units of 10^{-15} erg cm^{-2} s^{-1} .

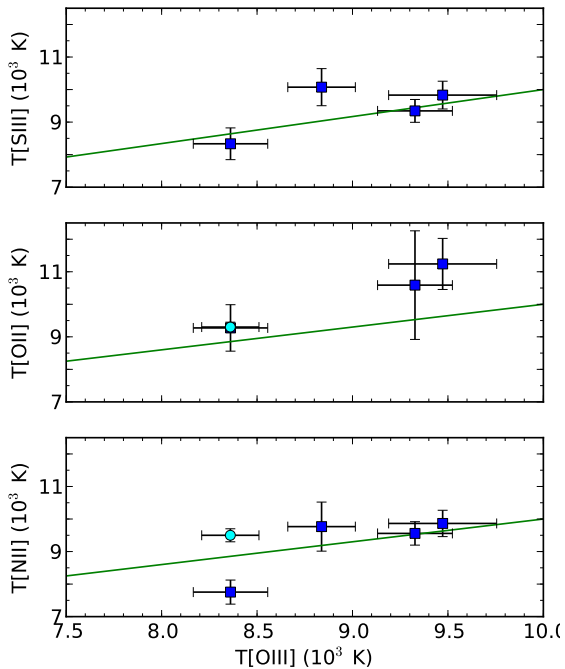


Figure 3. Comparison between the electron temperature obtained from the $[\text{O III}]\lambda 4363/[\text{O III}]\lambda\lambda 4959,5007$ line ratio and the electron temperatures obtained from $[\text{S III}]\lambda 6312/[\text{S III}]\lambda\lambda 9069,9532$ (top), $[\text{O II}]\lambda 7325/[\text{O II}]\lambda\lambda 3727,3729$ (middle), and $[\text{N II}]\lambda 5755/[\text{N II}]\lambda\lambda 6548,6584$ (bottom). The cyan circle corresponds to the H II region K932, studied by Esteban et al. (2009). The green straight lines indicate the relationship between different temperatures predicted by the Garnett (1992) models.

Four additional targets (#8, #14, #22 and #32) are SNR candidates. Targets #8 and #32 have a $[\text{S II}]/\text{H}\alpha$ ratio consistent with an H II region, but their spectra present numerous metal lines in the blue range (mainly from Fe and Mg), as well as relatively strong $[\text{O I}]\lambda\lambda 6300, 6360$. In addition, their $[\text{O II}]\lambda 4363$ emission appears to be contaminated by $[\text{Fe II}]\lambda 4359$. We suspect that these targets are young SNRs.

For targets with lower signal-to-noise spectra, we have tentatively identified as SNRs those with $[\text{S II}]/\text{H}\alpha \gtrsim 0.4$ and substantial $[\text{O I}]\lambda 6300$ emission, $[\text{O I}]\lambda 6300 \gtrsim 0.02$, (Dennefeld & Kunth 1981). According to this criteria, targets #14 and #22 are SNR candidates as well.

The six targets discussed in this section are removed from our sample and will not be considered in the remainder of the paper, since the application of H II region metallicity diagnostics would not be appropriate. For completeness we report their line fluxes in Table 4 (#5, #8, #29 and #32) and in Table 5 (#14 and #22).

3 PHYSICAL CONDITIONS OF THE IONIZED GAS

The physical conditions of the ionized gas (electron temperature and density) have been determined from collisionally excited line ratios. The `temden` IRAF task within the NEBULAR package (Shaw & Dufour 1995) was employed.

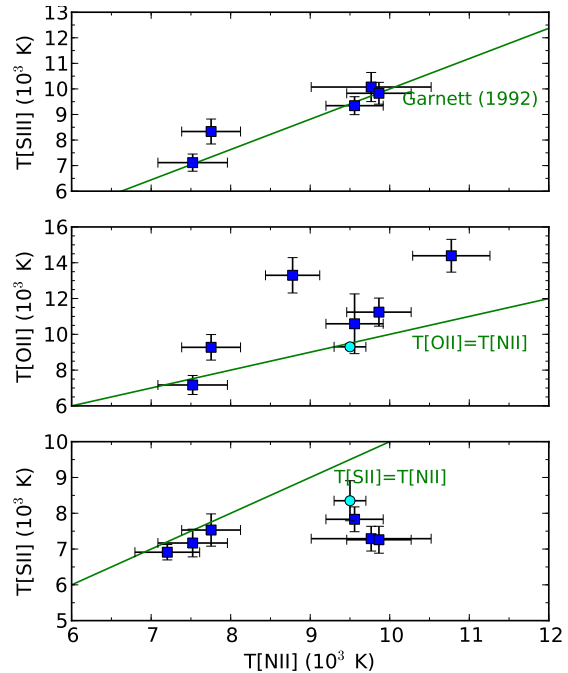


Figure 4. Comparison between the electron temperature obtained from the $[\text{N II}]\lambda 5755/[\text{N II}]\lambda\lambda 6548,6584$ line ratio and the electron temperatures obtained from $[\text{S III}]\lambda 6312/[\text{S III}]\lambda\lambda 9069,9532$ (top), $[\text{O II}]\lambda 7325/[\text{O II}]\lambda\lambda 3727,3729$ (middle) and $[\text{S II}]\lambda 4072/[\text{S II}]\lambda\lambda 6717,6731$ (bottom). The cyan circle corresponds to the H II region K932, studied by Esteban et al. (2009).

The `temden` task is an extension of the FIVEL program (De Robertis, Dufour, & Hunt 1987) for a larger set of ions, emission lines and number of levels (between 5 and 8 depending on the ion). The atomic parameters (transition probabilities and collisional strengths) for the ions of interest were updated with more recent data as shown in Table 5 of Bresolin et al. (2009a).

The derivation of the electron temperature of an H II region requires the detection of auroral lines which arise from the transition from the second lowest excited level to the lowest excited level. Auroral lines are generally faint and difficult to detect, with strongly decreasing intensities with increasing gas metallicity. This explains why, to our knowledge, there is surprisingly only one previous published measurement of electron temperature for an H II region in M31: region K932, analysed by Esteban et al. (2009) from Keck HIRES data. For nine H II regions of our sample, one or more of the auroral lines $[\text{O II}]\lambda 4363$, $[\text{S III}]\lambda 6312$, $[\text{O II}]\lambda 7325$, $[\text{N II}]\lambda 5755$ and $[\text{S II}]\lambda 4072$ have been detected. The ratio of these lines to stronger nebular lines of the same ions are highly dependent on electron temperature and can thus be employed for measuring it. The auroral line $[\text{N II}]\lambda 5755$ was detected in all nine H II regions, while $[\text{S III}]\lambda 6312$ was measured in only five. This is in part due to the fact that this emission line, due to the radial velocity of M31, is within 2 \AA of the telluric line $[\text{O I}]\lambda 6300 \text{ \AA}$, and its firm detection is therefore subject to higher uncertainties.

Density and temperature of the ionized gas have been simultaneously obtained from an iterative process. The tem-

Table 5. Reddening-corrected line fluxes relative to H β (with H β =100) for the H II regions with no detections of auroral lines.

ID	[O II] 3727	[O III] 4959	[O III] 5007	[N II] 6548	H α 6562	[N II] 6583	[S II] 6717	[S II] 6731	F(H β) (10^{-15} erg s $^{-1}$ cm $^{-2}$)	c(H β) (mag)
1	44 \pm 2	290 \pm 20	149 \pm 8	0.20 \pm 0.08	0.00
4	140 \pm 30	20 \pm 4	290 \pm 60	60 \pm 13	27 \pm 6	19 \pm 4	0.5 \pm 0.1	0.64
6	122 \pm 6	4.7 \pm 0.5	11.6 \pm 0.7	33 \pm 2	300 \pm 20	122 \pm 7	40 \pm 2	25 \pm 2	1.43 \pm 0.05	0.00
7	230 \pm 20	2.1 \pm 0.9	3.5 \pm 1.0	51 \pm 5	290 \pm 30	161 \pm 15	1.09 \pm 0.04	0.45
9	200 \pm 20	12 \pm 2	35 \pm 3	38 \pm 4	290 \pm 30	123 \pm 12	77 \pm 8	53 \pm 5	0.42 \pm 0.02	0.00
10	150 \pm 20	...	7 \pm 2	45 \pm 6	290 \pm 40	130 \pm 16	48 \pm 6	33 \pm 4	1.00 \pm 0.04	0.58
11	150 \pm 10	10.3 \pm 0.6	29.5 \pm 1.4	31 \pm 2	290 \pm 20	93 \pm 7	30 \pm 2	21 \pm 2	3.9 \pm 0.1	0.19
12	149 \pm 12	6.2 \pm 1.4	18 \pm 2	40 \pm 4	290 \pm 30	120 \pm 11	72 \pm 7	46 \pm 5	0.232 \pm 0.009	0.00
13	97 \pm 8	6.5 \pm 0.8	21 \pm 1	26 \pm 2	290 \pm 30	75 \pm 7	1.15 \pm 0.04	0.36
14*	390 \pm 50	...	16 \pm 3	29 \pm 6	280 \pm 50	100 \pm 20	90 \pm 20	69 \pm 13	0.56 \pm 0.04	0.59
15	180 \pm 20	12 \pm 4	27 \pm 4	30 \pm 5	280 \pm 50	80 \pm 13	47 \pm 8	29 \pm 5	0.68 \pm 0.03	0.64
16	94 \pm 8	...	4.6 \pm 0.8	18 \pm 2	290 \pm 30	67 \pm 6	36 \pm 4	24 \pm 2	0.58 \pm 0.02	0.00
18	193 \pm 20	39 \pm 4	300 \pm 30	124 \pm 12	72 \pm 7	50 \pm 5	0.68 \pm 0.03	0.68
20	130 \pm 8	6.6 \pm 0.6	18 \pm 1	25 \pm 2	290 \pm 20	73 \pm 5	31 \pm 2	21 \pm 2	8.9 \pm 0.3	0.90
21	126 \pm 7	3.2 \pm 0.4	7.9 \pm 0.5	27 \pm 2	290 \pm 20	83 \pm 5	29 \pm 2	20.2 \pm 1.4	8.5 \pm 0.3	0.98
22*	220 \pm 20	23 \pm 2	62 \pm 3	38 \pm 2	290 \pm 20	123 \pm 8	64 \pm 4	46 \pm 3	2.03 \pm 0.07	0.61
23	130 \pm 8	6.6 \pm 0.6	18.0 \pm 1.1	25 \pm 2	290 \pm 20	73 \pm 5	31 \pm 2	21 \pm 2	8.9 \pm 0.3	0.90
24	300 \pm 20	22.1 \pm 1.2	64 \pm 3	31 \pm 2	290 \pm 20	91 \pm 6	48 \pm 3	33 \pm 2	2.80 \pm 0.09	0.42
27	210 \pm 20	19 \pm 2	280 \pm 30	68 \pm 6	42 \pm 4	27 \pm 3	3.8 \pm 0.1	0.79
28	...	74.6 \pm 3.6	220 \pm 10	13.3 \pm 0.9	290 \pm 20	43 \pm 3	15 \pm 1	10.2 \pm 0.7	14.4 \pm 0.05	1.03
30	7.3 \pm 0.3	20.6 \pm 1.3	290 \pm 20	62 \pm 4	25 \pm 2	16.9 \pm 1.1	2.52 \pm 0.08	0.19
31	290 \pm 20	11.2 \pm 0.8	35 \pm 2	28 \pm 2	290 \pm 20	83 \pm 5	38 \pm 3	28 \pm 2	5.9 \pm 0.2	0.57
36	253 \pm 19	6.3 \pm 0.3	15.6 \pm 0.7	21 \pm 2	280 \pm 30	56.5 \pm 5	7.7 \pm 0.3	1.03
37	257 \pm 13	16.2 \pm 0.8	48 \pm 2	25 \pm 2	280 \pm 20	75 \pm 4	13.3 \pm 0.5	0.74

* SNRs candidates (see Sect. 2.4) for details.

Table 6. Measured H II region electron temperatures (in K) and densities (in cm $^{-3}$). The auroral line intensities [O II] λ 7325 and [N II] λ 5755 have been corrected for recombination contamination following Liu et al. (2000).

ID	T [O III] $\frac{4363}{4959+5007}$	T [S III]* $\frac{6312}{9069+9532}$	T [O II] $\frac{7325}{3727}$	T [N II] $\frac{5755}{6548+6583}$	T [S II] $\frac{4072}{6717+6731}$	N_e [S II] $\lambda\lambda$ 6717/6731
2	...	7100 \pm 300	7200 \pm 500	7500 \pm 400	7200 \pm 400	66
3	8300 \pm 300	...	49
17	8400 \pm 200	8300 \pm 500	9300 \pm 700	7800 \pm 400	7500 \pm 500	38
19	7200 \pm 400	6900 \pm 200	24**
25	9300 \pm 200	9300 \pm 400	10600 \pm 1700	9600 \pm 400	7800 \pm 300	28
26	9500 \pm 300	9800 \pm 400	11200 \pm 800	9900 \pm 400	7300 \pm 400	17**
33	13300 \pm 1000	8800 \pm 300	...	24
34	14400 \pm 900	10800 \pm 500	...	14**
35	8800 \pm 200	10100 \pm 600	...	9800 \pm 800	7300 \pm 300	80

* Assuming [S III] λ 9532/[S III] λ 9069=2.44.** [S II]6717/[S II]6731 line ratios slightly above 1.41 (1.44, 1.43 and 1.45 respectively); it has been assumed that [S II] λ 6717/[S II] λ 6731=1.41.

perature was initially set to $T_e=7500$ K and a preliminary value for the electron density N_e was derived from the [S II] λ 6717/[S II] λ 6731 line ratio. This initial value of N_e was then used for computing T_e for the different auroral-to-nebulular line ratios. The process was repeated until convergence. An initial estimate of the ionic abundances was then obtained (as described in Sect. 4.1) and from these we estimated the contamination of the auroral lines [N II] λ 5755 and [O II] λ 7325 due to recombination following Liu et al. (2000) (their Eqs. 1 and 2) and assuming $N^{++}/N^+ \simeq O^{++}/O^+$ to obtain N^{++}/H^+ . The electron temperatures and densities were recomputed until convergence after the correction for recombination contamination was applied. This correction is small and varies between 0.1 and 0.9% for [N II] λ 5755/H β and between 0.3 and 3.7% for [O II] λ 7325/H β . We note that

in a number of regions T [O II] is above the range of validity of the Liu et al. (2000) formula for [O II] λ 7325/H β (5000 K < T_e < 10000 K). In any case, the errors in the derived T [O II] value for these H II regions are significantly larger than the corresponding correction.

The electron temperatures are shown in columns 2 to 6 of Table 6. The errors reported for T_e arise from error propagation of the relevant line flux errors and are in the range 200–600 K for all ions, except in the case of T [O II], for which the errors are larger (400–1700 K). This is mainly due to the observational uncertainty that involves the measurement of the [O II] multiplet at 7325 Å, located in a spectral region of strong OH airglow emission.

Figs. 3 and 4 show a comparison between the different ionic temperatures we measured and the results one would

obtain from model predictions by Garnett (1992), frequently used for predicting ionic temperatures when only one or two auroral lines are detected. Fig. 3 shows the relations between $T[\text{S III}]$, $T[\text{O II}]$ and $T[\text{N II}]$ with respect to $T[\text{O III}]$. For most of the regions with a $T[\text{O III}]$ determination, the Garnett (1992) temperature relations

$$T[\text{S III}] = 0.83T[\text{O III}] + 1700\text{K} \quad (1)$$

$$T[\text{O II}] = T[\text{N II}] = 0.70T[\text{O III}] + 3000\text{K} \quad (2)$$

appear to be satisfactorily followed by the empirical data, especially for the case of $T[\text{S III}]$ vs. $T[\text{O III}]$. In the other two cases the data points deviate more significantly from the theoretical relations. This was also found by other authors with a larger sample of H II regions (e.g. Kennicutt, Bresolin, & Garnett 2003; Pérez-Montero & Díaz 2003).

Fig. 4 shows the relations between the different ionic temperatures with respect to $T[\text{N II}]$, and highlights a result already found by other authors (e.g. Bresolin et al. 2005): $T[\text{O II}]$ seems to overestimate the temperature with respect to $T[\text{N II}]$, while the opposite happens to $T[\text{S II}]$, which gives always lower temperatures than $T[\text{N II}]$. However, $T[\text{S III}]$ seems to be well correlated with $T[\text{N II}]$, following closely the model predictions by Garnett (1992).

The electron densities N_e are shown in column 7 of Table 6. All H II regions are in the low-density regime, with densities below 100 cm^{-3} . For three H II regions we measured a line ratio $[\text{S II}]\lambda 6717/[\text{S I}]\lambda 6731$ slightly above the theoretical limit. For those regions we assumed a line ratio equal to 1.41 (equivalent to the theoretical limit).

4 CHEMICAL ABUNDANCES

4.1 Ionic abundances

The calculation of ionic abundances from collisionally-excited lines requires a good knowledge of the electron temperature. An onion-model is commonly adopted to describe the ionization structure of an H II region, with a number of zones of different T_e where atomic species of similar excitation coexist. In light of the correlations found in Sec. 3 between the T_e obtained from different atomic species, we have adopted a two-zone representation for describing the temperature stratification of the H II regions: a low-excitation zone, characterized by $T[\text{N II}]$, where ions of low ionization potential coexist (O^+ , S^+ , N^+) and a high-excitation zone for the ions with higher ionization potential (O^{++} , S^{++} , Ar^{++} , Ne^{++}), characterized by $T[\text{O III}]$. For the H II regions for which we could not measure $T[\text{O III}]$, we have used the average of our measured value for $T[\text{S III}]$, and the value for $T[\text{O III}]$ obtained from the measured $T[\text{N II}]$ by inverting Eq. 2 (Garnett 1992). When $T[\text{S III}]$ was not available, $T[\text{O III}]$ has been obtained from $T[\text{N II}]$ and the mentioned relation (Eq. 2). Table 7 contains the temperatures adopted for the ionic abundance calculation for each H II region. The errors quoted in the table correspond to the errors in the measured values for $T[\text{N II}]$ and $T[\text{O III}]$, as described in Sect. 3, when these temperatures were available. When the Garnett relations were used, the uncertainty in $T[\text{O III}]$ comes from error propagation of the uncertainty in $T[\text{N II}]$, $T[\text{S III}]$ and

Table 7. Adopted electron temperatures for the two-zone scheme of the H II region ionization structure.

ID	$T[\text{O}^+, \text{N}^+, \text{S}^+]$ (K)	$T[\text{S}^{++}, \text{Ar}^{++}, \text{O}^{++}, \text{Ne}^{++}]$ (K)
2	7500 ± 400	6800 ± 400
3	8300 ± 300	7600 ± 600
17	7800 ± 400	8400 ± 200
19	7200 ± 400	6000 ± 700
25	9600 ± 400	9300 ± 200
26	9900 ± 400	9500 ± 300
33	8800 ± 300	8300 ± 600
34	10800 ± 500	11100 ± 800
35	9800 ± 800	8800 ± 200

an additional term added in quadrature, which is an estimate of the uncertainty in the scaling relation ($\pm 400\text{K}$ for $T[\text{N II}]$ vs. $T[\text{O III}]$) obtained from works with a large number of H II regions (Bresolin et al. 2009a).

The ionic IRAF task within the NEBULAR package (Shaw & Dufour 1995) was employed for obtaining the ionic abundances of O^+ , O^{++} , N^+ , S^+ , S^{++} , Ar^{++} and Ne^{++} . They were estimated from the relevant reddening-corrected emission line ratios from those species (Table 4) and the corresponding electron temperatures of the adopted two-zone scheme (Table 7). Table 8 shows the resulting ionic abundances with respect to H^+ .

4.2 Total abundances

The total abundance relative to hydrogen of a given element is given by the sum of the abundances of all its ions. However, not all ions have emission lines in our spectra and we have to correct for these unseen ionization stages using ionization correction factors (ICFs). We have used the following common assumptions:

Oxygen. $\text{He II } \lambda 4686$ is only detected in one target (#8) which is a SNR. This implies that all H II regions are of sufficiently low excitation that the amount of oxygen in ionization stages higher than O^{++} is negligible. We have therefore set $\text{O}/\text{H} = \text{O}^+/\text{H}^+ + \text{O}^{++}/\text{H}^+$.

Nitrogen and Neon. For these elements we have assumed that $\text{N}/\text{O} = \text{N}^+/\text{O}^+$ and $\text{Ne}/\text{O} = \text{Ne}^{++}/\text{O}^{++}$, which result from ionization potential considerations of the ions involved (see Bresolin et al. 2009a).

Argon. Only Ar^{++} is observed in our optical spectra. However, the amount of Ar^+ in low excitation H II regions (our case) can be important (Bresolin, Garnett, & Kennicutt 2004). We have employed the ICFs obtained from photoionization models by Izotov et al. (2006). These authors proposed different parameterizations depending on metallicity. Those for high ($12 + \log(\text{O}/\text{H}) > 8.2$) and intermediate ($7.6 < 12 + \log(\text{O}/\text{H}) \leq 8.2$) metallicity cover our range of oxygen abundances:

$$\text{ICF}(\text{Ar}^{++}) = \begin{cases} 0.285v + 0.833 + 0.051/v & \text{intermediate Z} \\ 0.517v + 0.763 + 0.042/v & \text{high Z} \end{cases} \quad (3)$$

where $v \equiv \text{O}^+ / (\text{O}^+ + \text{O}^{++})$.

Sulfur. In the case of low excitation H II regions the ICF to correct $(\text{S}^+ + \text{S}^{++})/\text{H}^+$ for the presence of higher ionization sulfur stages is expected to be small. We have used

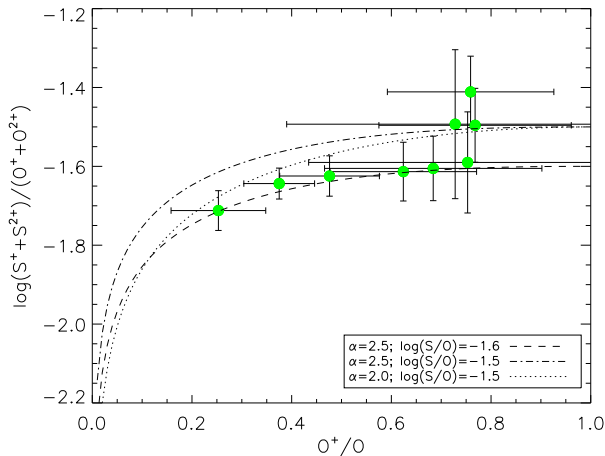
Table 8. O^+/O and ionic abundances (columns 3 to 9) given as $12 + \log(X/H)$, where X is the ion in the table header.

ID	O^+/O	O^+	O^{++}	N^+	S^+	S^{++}	Ne^{++}	Ar^{++}
2	0.8 ± 0.3	8.50 ± 0.14	8.02 ± 0.13	7.56 ± 0.09	6.30 ± 0.08	6.95 ± 0.07	7.21 ± 0.16	6.22 ± 0.09
3	0.8 ± 0.2	8.16 ± 0.07	7.66 ± 0.14	7.41 ± 0.04	6.16 ± 0.04	6.78 ± 0.08	...	6.06 ± 0.10
17	0.7 ± 0.2	8.25 ± 0.11	7.92 ± 0.04	7.40 ± 0.07	6.07 ± 0.06	6.73 ± 0.02	7.03 ± 0.05	6.11 ± 0.03
19	0.7 ± 0.3	8.49 ± 0.15	8.06 ± 0.31	7.70 ± 0.09	6.46 ± 0.08	7.03 ± 0.16	...	6.36 ± 0.21
25	0.4 ± 0.1	7.86 ± 0.07	8.08 ± 0.03	6.83 ± 0.05	5.68 ± 0.04	6.59 ± 0.02	7.34 ± 0.04	6.03 ± 0.02
26	0.5 ± 0.1	7.95 ± 0.08	8.00 ± 0.05	6.98 ± 0.05	5.85 ± 0.04	6.58 ± 0.03	7.26 ± 0.06	6.01 ± 0.03
33	0.8 ± 0.2	8.17 ± 0.08	7.65 ± 0.14	7.29 ± 0.05	6.18 ± 0.05	6.67 ± 0.08	...	5.91 ± 0.09
34	0.6 ± 0.1	7.90 ± 0.08	7.68 ± 0.10	7.19 ± 0.05	6.13 ± 0.05	6.24 ± 0.06	6.63 ± 0.12	5.93 ± 0.07
35	0.3 ± 0.1	7.80 ± 0.16	8.27 ± 0.03	6.84 ± 0.09	5.72 ± 0.09	6.64 ± 0.02	7.55 ± 0.04	6.13 ± 0.02

Table 9. Total abundances.

ID	$12 + \log(O/H)$	$\log(N/O)$	$\log(S/O)$	$\log(Ar/O)$	$\log(Ne/O)$	He/H	R/R_{25}^*
2	8.62 ± 0.11	-0.95 ± 0.17	-1.58 ± 0.13	-2.32 ± 0.14	-0.81 ± 0.20	0.098 ± 0.027	0.40
3	8.28 ± 0.06	-0.76 ± 0.08	-1.41 ± 0.09	-2.14 ± 0.12	...	0.111 ± 0.024	0.42
17	8.42 ± 0.08	-0.86 ± 0.13	-1.59 ± 0.08	-2.23 ± 0.08	-0.89 ± 0.06	0.111 ± 0.017	0.44
19	8.63 ± 0.14	-0.79 ± 0.17	-1.49 ± 0.19	-2.19 ± 0.25	...	0.083 ± 0.034	0.46
25	8.28 ± 0.04	-1.02 ± 0.09	-1.58 ± 0.04	-2.23 ± 0.04	-0.74 ± 0.05	0.088 ± 0.005	0.71
26	8.28 ± 0.04	-0.98 ± 0.09	-1.59 ± 0.05	-2.23 ± 0.06	-0.73 ± 0.07	0.090 ± 0.006	0.71
33	8.29 ± 0.07	-0.89 ± 0.10	-1.49 ± 0.09	-2.30 ± 0.12	...	0.074 ± 0.015	0.76
34	8.10 ± 0.06	-0.71 ± 0.10	-1.60 ± 0.07	-2.14 ± 0.09	-1.05 ± 0.16	0.089 ± 0.004	0.75
35	8.40 ± 0.05	-0.96 ± 0.18	-1.60 ± 0.05	-2.24 ± 0.05	-0.72 ± 0.05	0.087 ± 0.005	0.76

* Deprojected galactocentric distance normalized to R_{25} . See Table 2 for the M31 adopted parameters.

**Figure 5.** Logarithm of $(S^+ + S^{++})/(O^+ + O^{++})$ versus O^+/O for our H II region sample (filled circles). The lines show the sulfur ionization correction factor (Eq. 4) for different values of α and assuming a constant value for $\log(S/O)$.

the ICF given by the formula (Peimbert & Costero 1969; Stasińska 1978; French 1981):

$$ICF(S^+ + S^{++}) = \frac{S}{S^+ + S^{++}} = \left[1 - \left(1 - \frac{O^+}{O} \right)^\alpha \right]^{-1/\alpha} \quad (4)$$

where we have employed $\alpha = 2.5$ (Bresolin et al. 2004). Fig. 5 shows $\log[(S^+ + S^{++})/(O^+ + O^{++})]$ for our H II region sample versus the oxygen fractional ionization O^+/O . Eq. 4 has been overplotted for $\alpha = 2$ and $\alpha = 2.5$ and assuming $\log(S/O) = -1.5$ and $\log(S/O) = -1.6$ (representative values for our sample). Apart from three low-excitation

regions with considerable error bars, the curve with $\alpha = 2.5$ and $\log(S/O) = -1.6$ follows the data rather well. We have then kept this parameter choice, in agreement with previous work on extragalactic H II regions (Kennicutt et al. 2003; Bresolin et al. 2004). This equation yields corrections of 16-30% for the highest excitation H II regions of the sample ($O^+/O \sim 0.25-0.4$), 2-9% for H II regions with $O^+/O \sim 0.5-0.7$, and corrections around 1% for the lowest excitation regions with $O^+/O \sim 0.8$.

The total abundances of O, N, S, Ar and Ne, obtained as described above, are summarized in Table 9.

4.3 Abundance trends with $\log(O/H)$ and galactocentric radius

Fig. 6 shows the total abundances of nitrogen, sulfur, neon and argon with respect to oxygen as a function of the oxygen abundances. The N/O ratio does not show the typical increase with $12 + \log(O/H)$ expected for a pure secondary origin of nitrogen (Vila-Costas & Edmunds 1993). The plot has a considerable scatter (~ 0.11 dex) around a mean corresponding to the solar value, $\log(N/O)_\odot = -0.86$ (Lodders 2003), and seems more compatible with a primary-plus-secondary origin for this element. The dispersion found in this relation is often explained as due to a time delay between the release of nitrogen and the release of oxygen back into the interstellar medium by the respective stellar sources (Vila-Costas & Edmunds 1993; Mallery et al. 2007). Also H II regions in the galaxy M33 display an approximately constant value of the N/O ratio (Bresolin et al. 2010), with a mean $\log(N/O) \sim -1.2$, i.e. between the solar value and typical values for dwarf galaxies. The flat radial distribution of the N/O ratio is shown in the top panel of Fig. 7.

The S/O ratio is constant as a function of $12 + \log(O/H)$, with a mean value $\log(S/O) = -1.55 \pm 0.07$, consis-

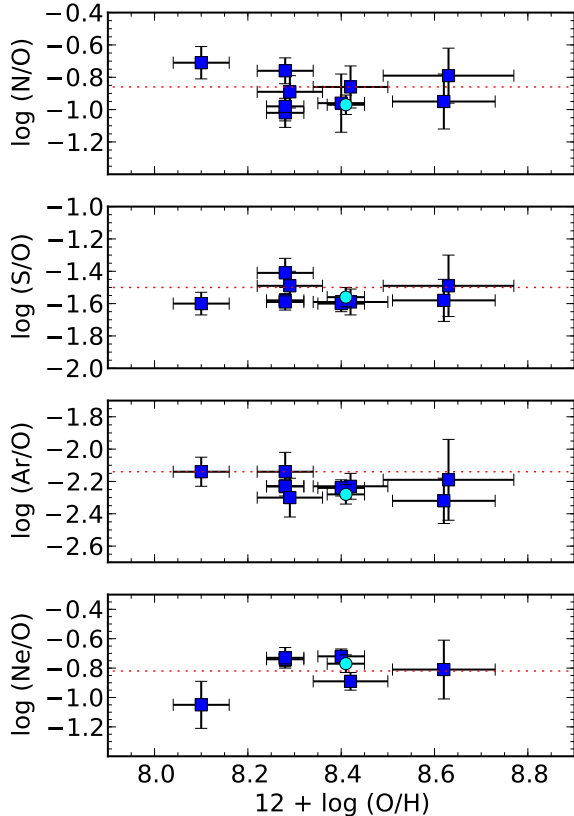


Figure 6. Trends in the abundance ratios relative to oxygen with $12+\log(\text{O}/\text{H})$. The horizontal dotted lines indicate the corresponding solar value according to Lodders (2003). The filled circle corresponds to the H II region K932 with abundances measured by Esteban et al. (2009).

tent, within errors, with the solar value (-1.50 ± 0.06 , Lodders 2003). The Ar/O ratio is also essentially constant with oxygen abundance, but with a mean value of $\log(\text{Ar}/\text{O}) = -2.22 \pm 0.06$, slightly subsolar but marginally compatible with the solar value (-2.14 ± 0.09 , Lodders 2003) within the uncertainties. The Ne/O ratio, with a mean value of $\log(\text{Ne}/\text{O}) = -0.82$ and a standard deviation of ~ 0.13 dex also shows a rather flat distribution in the whole range of oxygen abundance measured in our sample of H II regions, and matches the solar value (-0.82 ± 0.11 , Lodders 2003).

Our data are compatible with a flat distribution of the S/O, Ar/O and Ne/O ratios with galactocentric distance (see Figure 7), but since our H II region data are concentrated at only two different galactocentric distances further data would be required to confirm these trends.

4.4 He abundance

Our H II region spectra contain a number of He I recombination emission lines that can be used to estimate the He⁺ abundance, as the emission line is proportional to the line emissivity and to the corresponding ionic abundance. He II $\lambda 4686$ is not detected in any H II region of the sample and therefore the contribution of He⁺⁺ to the total He abundance can be neglected.

The ionic helium abundance relative to hydrogen has

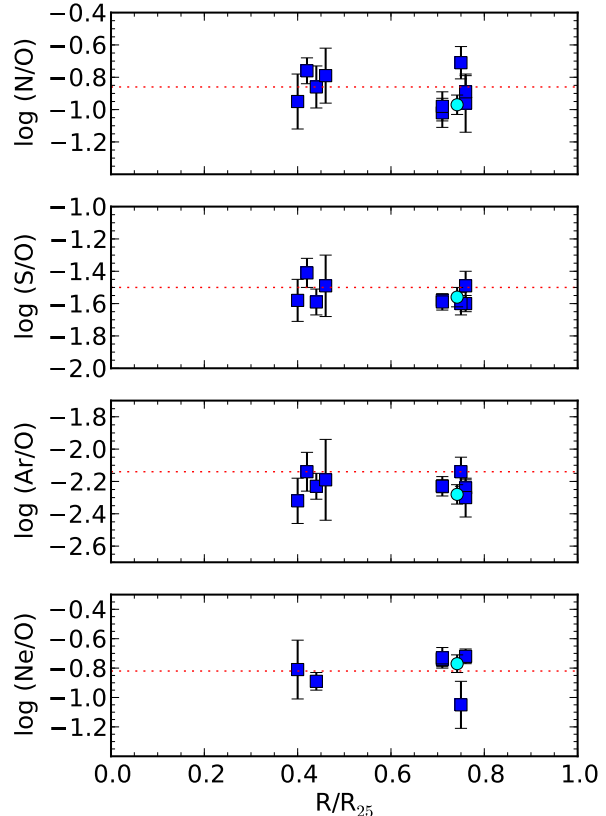


Figure 7. Trends in the abundance ratios relative to oxygen with galactocentric radius. The horizontal dotted lines indicate the corresponding solar value according to Lodders (2003). The filled circle corresponds to the H II region K932 with abundances measured by Esteban et al. (2009).

been computed from the predicted emissivities for the He I lines (Porter, Ferland, & MacAdam 2007) and for H β (Benjamin et al. 1999) at the corresponding H II region electron temperature, as computed in Sect. 4.1.

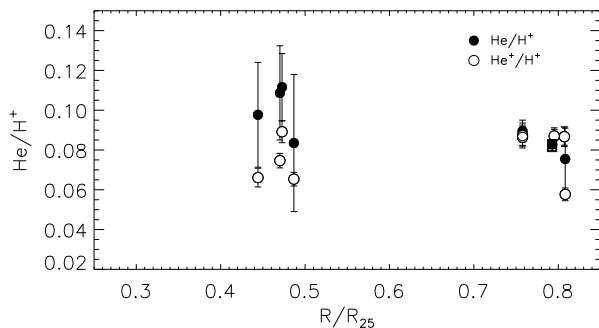
The He I emission lines are affected by underlying stellar absorption, which needs to be corrected for. We have followed the approach described by Kennicutt et al. (2003). The corrections are based both on direct measurements of the He I EWs for O-type stars and He I EWs predicted by starburst models as a function of age. We have applied here the same corrections as Kennicutt et al. (2003), except for He I $\lambda 4026$ (0.6 \AA) and He I $\lambda 4922$ (0.3 \AA), which have been estimated from more recent models (González-Delgado et al. 2005). These corrections range from $\sim 1\%$ to 6% for the brightest lines ($\lambda 5876$ and $\lambda 6678$), $\sim 6\text{-}30\%$ for $\lambda 4922$, and $\sim 2\text{-}40\%$ for $\lambda 4471$.

The He⁺ abundances computed from the brightest observed He I lines ($\lambda 4026$, $\lambda 4471$, $\lambda 4922$, $\lambda 5876$, $\lambda 6678$) are shown in Table 10, together with the weighted average (column 7) of all the individual values. The He⁺ abundances have also been computed using the Benjamin et al. (1999) emissivities. Differences in the abundances derived using the more recent Porter et al. (2007) emissivities are on average $\sim 2\%$, and in all cases below 5% and therefore below the He⁺/H⁺ abundance uncertainties.

The total helium abundances have been computed with

Table 10. He⁺ abundance.

ID	He ⁺ /H ⁺					Average ^a
	λ4026	λ4471	λ4922	λ5876	λ6678	
2	0.056 ± 0.005	0.063 ± 0.006	0.066 ± 0.006	0.069 ± 0.010	0.071 ± 0.009	0.066 ± 0.004
3	...	0.074 ± 0.006	0.076 ± 0.006	0.075 ± 0.007	0.079 ± 0.007	0.076 ± 0.003
17	0.086 ± 0.010	0.081 ± 0.008	0.086 ± 0.008	0.094 ± 0.011	0.089 ± 0.011	0.088 ± 0.005
19	...	0.060 ± 0.004	...	0.067 ± 0.006	0.068 ± 0.006	0.065 ± 0.003
25	0.082 ± 0.007	0.083 ± 0.007	0.085 ± 0.007	0.088 ± 0.008	0.087 ± 0.008	0.086 ± 0.004
26	0.083 ± 0.010	0.088 ± 0.011	0.092 ± 0.010	0.088 ± 0.011	0.088 ± 0.010	0.088 ± 0.005
33	...	0.058 ± 0.006	...	0.054 ± 0.006	0.058 ± 0.006	0.057 ± 0.003
34	...	0.093 ± 0.007	...	0.092 ± 0.007	0.081 ± 0.007	0.089 ± 0.004
35	0.094 ± 0.008	0.087 ± 0.008	...	0.084 ± 0.010	0.087 ± 0.010	0.087 ± 0.005

^a Weighted average of the He⁺/H⁺ abundance ratio computed from all He I lines in the table (λ4026, λ4471, λ4922, λ5876, λ6678).**Figure 8.** Total He abundance versus galactocentric distance (black filled circles) for our H II region sample. The ionic He⁺/H⁺ abundances are plotted with open circles. The total and ionic He abundances of the H II region K932 analysed by Esteban et al. (2009) are marked with a filled and open square, respectively.

the analytical relation between the ICF(He) and the softness parameter, $\eta = (O^+/O^{2+})/(S^+/S^{2+})$ (Vílchez & Pagel 1988), obtained by Bresolin et al. (2009a) from models of Stasińska, Schaerer, & Leitherer (2001). The ICF(He) ranges from 1.0 to 1.48 for our H II region sample. The resulting total He abundances are shown in column 7 of Table 9 and plotted versus galactocentric radius in Fig. 8. The figure includes region K932 (Esteban et al. 2009), which is in very good agreement with our data for similar galactocentric radius. The He abundance appears to be constant within our range of galactocentric distances, with an average value $He/H^+ = 0.092 \pm 0.012$, where the error represents the standard deviation between all regions.

5 OXYGEN RADIAL ABUNDANCE GRADIENT

The H II region oxygen abundances in M31 obtained in this paper from the direct T_e -based method are plotted as a function of galactocentric radius in Fig. 9 (blue squares). The linear regression to this data plus the H II region K932 by Esteban et al. (2009) yields the following solution:

$$12 + \log(O/H) = 8.72(\pm 0.18) - 0.028(\pm 0.014) \times R \text{ (kpc)} \quad (5)$$

or equivalently,

$$12 + \log(O/H) = 8.72(\pm 0.18) - 0.56(\pm 0.28) \times (R/R_{25}) \quad (6)$$

The slope that we obtain, $-0.028 \pm 0.014 \text{ dex kpc}^{-1}$, represents a rather shallow oxygen abundance gradient in M31. The central abundance is only slightly above solar ($12 + \log(O/H)_\odot = 8.69$, Asplund et al. 2009). We are aware that our data are virtually representative of only two distinct galactocentric distances, and further data at different distances from the M31 center would be desirable to better determine the abundance gradient from the T_e -based method alone.

This is the first time that an oxygen abundance gradient from auroral lines is obtained for M31. Previous attempts to measure the oxygen abundance gradient in this galaxy from H II regions were performed from diagnostics based on strong emission lines, because of the lack of the faint auroral lines necessary to measure the electron temperatures. The early papers by Dennefeld & Kunth (1981) and Blair et al. (1982) contain H II region samples of similar sizes (8 and 11 regions, respectively) and make use of empirical calibrations of the [O III]/[N II] line ratio (Alloin et al. 1979) and the R_{23} parameter ($R_{23} = ([O III] + [O II])/H\beta$, Pagel et al. 1979) to derive the T_e from which the O/H is estimated. Their O/H vs. galactocentric radius relations have a lot of scatter, but are in agreement with each other and seem compatible with super-solar oxygen abundance in the M31 center ($12 + \log(O/H) > 9.1$) and an abundance gradient with a slope of approximately -0.03 dex kpc (from Fig. 4 and Fig. 6. of Dennefeld & Kunth (1981) and Blair et al. (1982), respectively). This value is in agreement with our slope, but their metallicities are about 0.5 dex systematically higher than our determinations.

Additional authors have recalculated the oxygen abundance gradient in M31, by applying different calibrations of the R_{23} parameter to the data obtained by Dennefeld & Kunth (1981) and Blair et al. (1982). Vila-Costas & Edmunds (1992) used the R_{23} calibration by Edmunds & Pagel (1984), with adjustments at high and low metallicities (Edmunds 1989; Skillman 1989). They obtained a somewhat steeper slope $-0.043 \text{ dex kpc}^{-1}$. In contrast, Zaritsky et al. (1994), using the same dataset, obtained a shallower abundance gradient ($-0.018 \pm 0.006 \text{ dex kpc}^{-1}$) with a combination of three different calibrations of the R_{23} parameter (Edmunds & Pagel 1984; Dopita & Evans 1986; McCall, Rybski, & Shields 1985). In both cases a super-

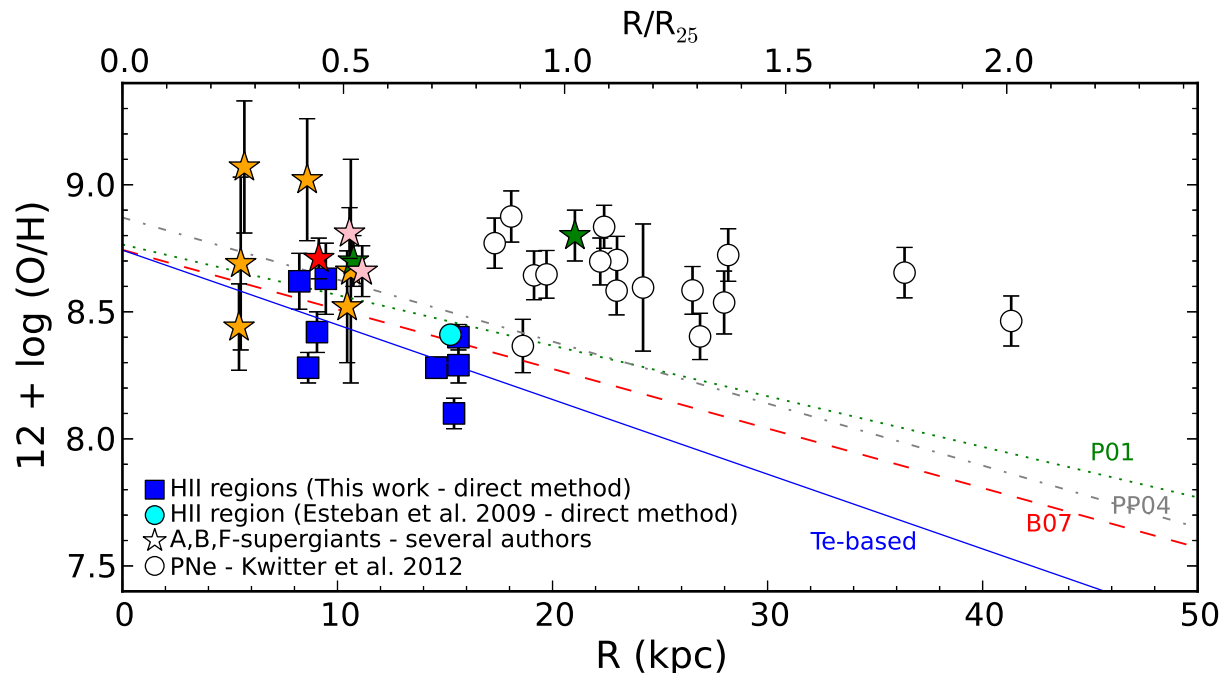


Figure 9. Radial metallicity gradient from the *direct* T_e -based method obtained from our work (filled blue squares). A direct abundance measurement from Esteban et al. (2009) for H II region K932 is indicated with a cyan circle. A-, B- and F-supergiant oxygen abundances from different authors are indicated with filled yellow (Trundle et al. 2002), green (Venn et al. 2000), red (Smartt et al. 2001) and pink (Przybilla et al. 2006) stars. We also include the recent oxygen abundance determination for M31 PNe by Kwitter et al. (2012) with open dots. The solid straight line shows the best linear fit to the H II region *direct* oxygen abundance versus galactocentric radius (see Sect. 5), while the dotted, dashed and dot-dashed straight lines show the best linear fits to the oxygen abundances obtained from the Pilyugin (2001), Bresolin (2007) and Pettini & Pagel (2004) strong-line methods, respectively, applied to the whole sample of H II regions available in the literature (see Sect. 5.1).

solar central abundances (again $12+\log(\text{O}/\text{H}) > 9.1$) was obtained.

The most recent spectroscopic observations of a sample of H II regions in M31 were performed by Galarza et al. (1999). Their sample comprises 46 H II regions which the authors classify according to their morphological type. These authors inferred a metallicity gradient of $-0.06 \pm 0.03 \text{ dex kpc}^{-1}$ from the dependence of the R_{23} parameter of the regions classified as *center-brightened* (~ 20 H II regions) with the radial distance from the galaxy center. This gradient is steeper compared to our and previous determinations of the oxygen abundance gradient of M31, but given its large uncertainty this result is still compatible with the shallower slope we find. Further spectroscopic observations of six H II regions in M31 were obtained by Bresolin et al. (1999), but for a different purpose, and no abundance estimations were performed.

More recent published values of the M31 oxygen abundance gradient from H II regions come from the reanalysis of the datasets described above (Dennefeld & Kunth 1981; Blair et al. 1982; Galarza et al. 1999) using different empirical calibrations (Pagel, Edmunds, & Smith 1980; McGaugh 1991; Zaritsky et al. 1994; Pilyugin 2001). Depending on the empirical calibration applied, the slope ranges from -0.013 to $-0.027 \text{ dex kpc}^{-1}$, and the central abundance varies between 8.70 and 9.20 dex (Smartt et al. 2001; Trundle et al. 2002).

5.1 Strong-line methods

The previous section makes it clear that the usage of different calibrations of ratios of bright nebular emission lines (*strong-line methods*), which are readily accessible observationally to determine the oxygen abundance gradient from a given data set, yields systematic and non-negligible differences on both the metallicity gradient and on the central ($R=0 \text{ kpc}$) oxygen abundance. This is well known from the detailed analysis of different galaxies from many authors (e.g. Pérez-Montero & Díaz 2005; Kewley & Ellison 2008; Bresolin et al. 2009a,b; López-Sánchez & Esteban 2010). In particular, strong-line methods calibrated via grids of photoionization models generally provide higher metallicities than those calibrated empirically via sets of H II region oxygen abundance determinations obtained from T_e estimates from detected auroral lines.

Given the still limited number of regions for which we have a direct determination of the electron temperature in M31, it is useful to apply different bright-line metallicity indicators to the whole set of M31 H II regions observed so far to enlarge the range in galactocentric distance and the number of regions for a better statistical significance of the gradient parameters. As a first step, we have applied strong-line methods to the whole set of 31 H II regions analyzed in this paper (those with and without detections of auroral lines), limiting our choice to six widely used methods: (a) The R_{23} method, as calibrated empirically by Pilyugin (2001, P01) and Pilyugin & Thuan (2005,

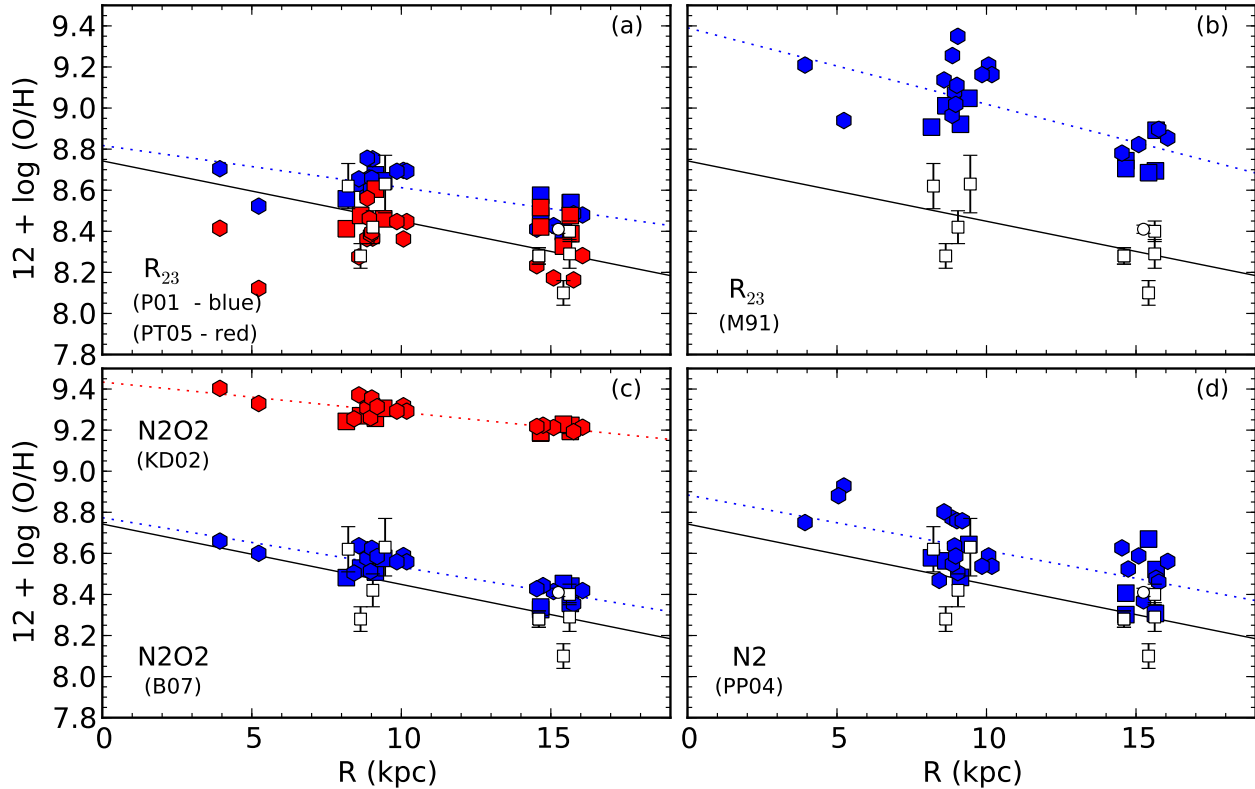


Figure 10. Radial oxygen abundance gradient in M31 from different calibrations of strong-line ratios applied to the H II regions analyzed in this paper (filled symbols): (a) Pilyugin (2001, P01) and Pilyugin & Thuan (2005, PT05) empirical calibrations of the R_{23} indicator. (b) R_{23} strong-line method as calibrated by McGaugh (1991). (c) N2O2 ($=[\text{N II}]/[\text{O II}]$) as calibrated by Bresolin (2007, B07) and Kewley & Dopita (2002, KD02) (d) N2 $=\log([\text{N II}]\lambda 6583/\text{H}\alpha)$ as empirically calibrated by Pettini & Pagel (2004, PP04). The dotted straight lines show the best linear fit to the oxygen abundance gradient obtained from the corresponding strong-line methods. The fit parameters are shown in Table 11. The solid straight line shows the best fit to the oxygen abundances obtained from direct measurements of T_e (Eq. 5). Filled squares indicate H II regions with detections of auroral lines, while filled hexagons indicate regions with no detections of auroral lines. The open symbols show the direct T_e -based oxygen abundances derived in this paper.

PT05) from spectroscopic data of H II regions with measured T_e -based oxygen abundances. (b) The R_{23} method, as calibrated from theoretical model grids by McGaugh (1991, M91), through the Kuzio de Naray, McGaugh, & de Blok (2004) parametrization, which takes into account the ionization parameter of the H II regions. (c) The N2O2 method, i.e. the empirical calibration of the $[\text{N II}]\lambda 6583/[\text{O II}]\lambda 3727$ line ratio by Bresolin (2007, B07) with extragalactic H II regions with T_e -based oxygen abundances, and the calibration obtained by Kewley & Dopita (2002) from stellar population synthesis and photoionization models. (d) The N2 $\equiv \log([\text{N II}]\lambda 6583/\text{H}\alpha)$ method, empirically calibrated by Pettini & Pagel (2004, PP04) with H II regions with T_e -based oxygen abundances or detailed photoionization modelling.

The results from the application of these methods to our H II region sample are plotted in Fig. 10 as a function of the galactocentric radius. For the three R_{23} -based calibrations we have used the upper branch, as indicated by the discriminator $[\text{N II}]\lambda 6583/[\text{O II}]\lambda 3727$ (Kuzio de Naray et al. 2004; Kewley & Ellison 2008). For comparison we also plot (with open symbols) the T_e -based oxygen abundances derived in this paper together with the best linear fit to the data (solid line). The oxygen abundances obtained with the R_{23} param-

eter as calibrated by McGaugh (1991) and the ones obtained with the N2O2 calibration of Kewley & Dopita (2002) are ~ 0.4 - 0.7 dex larger than the ones obtained from the other methods, as expected when comparing empirical and theoretical model grid calibrations. Table 11 shows the best linear fit parameters for the oxygen gradient obtained from the different strong-line methods.

It is apparent from Fig. 10 and Table 11 that the scatter varies between the different O/H indicators, being larger for the R_{23} -based methods and N2, and smaller in the case of N2O2 which presents the highest correlation coefficient (around -0.85 for both calibrations of N2O2, with a root mean squared (*rms*) residual scatter from the fit of 0.05 dex and 0.03 dex for the Bresolin (2007) and Kewley & Dopita (2002) calibrations, respectively (cf. 0.12 dex for N2 and for the PT05 calibrations and 0.14 dex for R_{23} as calibrated by McGaugh 1991).

Fig. 10 and Table 11 show that the slope of the oxygen abundance gradient obtained from the Pilyugin (2001) calibration of the R_{23} parameter, from N2, and from N2O2 as calibrated by Bresolin (2007) agree within the errors, and also agree with the oxygen abundance gradient obtained from the direct T_e -based oxygen abundances obtained in this paper. The McGaugh (1991) calibration of

the R_{23} parameter agrees marginally with the N2 calibration and with the T_e -based oxygen gradient. The N202 method as calibrated by Kewley & Dopita (2002) and the Pilyugin & Thuan (2005) calibration give shallower oxygen abundance gradients, but we note that the correlation of the abundances from the Pilyugin & Thuan (2005) method with galactocentric radius is poor (correlation coefficient ~ -0.2).

The six strong-line methods have also been applied to all spectroscopic data available in the literature for H II regions in M31 (Dennefeld & Kunth 1981; Blair et al. 1982; Galarza et al. 1999; Bresolin et al. 1999; Esteban et al. 2009). The galactocentric distances have been recalculated from their corresponding equatorial coordinates (as reported by the various authors) and using the same galactic parameters as for the estimation of the galactocentric distances of our H II region sample (see Table 2). Only the H II regions morphologically classified as *center-brightened* from the Galarza et al. (1999) sample have been considered. We also note that these authors and Bresolin et al. (1999) only provide the total [N II] λ 6548+ λ 6583 emission. In order to apply the N2 and the N2O2 methods to these samples, we have estimated the expected [N II] λ 6583 emission by assuming [N II] λ 6583 = $3 \times$ [N II] λ 6548. Also, in the cases in which [O III] λ 4959 is not detected, we assumed that [O III] λ 4959+5007=(4/3) [O III] λ 5007. The full H II region sample comprises 85 objects.

The results are plotted in Fig. 11 and the corresponding least-square fits parameter shown in Table 11. We obtain a similar behaviour as for our data alone: we observe an agreement between the T_e -based oxygen gradient and the slopes obtained from strong-line methods with the exception of the Pilyugin & Thuan (2005) empirical calibration and the N2O2 as calibrated by Kewley & Dopita (2002). These methods yield a substantially shallower slope (-0.009 ± 0.005 and -0.011 ± 0.002 dex kpc^{-1} , respectively). In the case of the Pilyugin & Thuan (2005) calibration, we find again that the correlation is poor (correlation coefficient -0.24). This lack of agreement of the Pilyugin & Thuan (2005) calibration with the T_e -based oxygen abundances is surprising and it is in contradiction with López-Sánchez & Esteban (2010), who conclude that the Pilyugin & Thuan (2005) calibration is nowadays the best empirical method to estimate oxygen abundances when auroral lines are not detected.

We should note that in all empirical calibrations we slightly improve the correlation coefficient and the scatter when the Galarza et al. (1999) sample is not taken into account, but the slope and intercept of the fits remain unchanged.

We have computed the weighted average of the slope of the oxygen abundance gradient from the strong-line methods with lower scatter and with a better match with our direct T_e -based oxygen abundances (i.e. with the N2O2 method as calibrated by Bresolin 2007, the N2 calibrated by Pettini & Pagel 2004, and the Pilyugin 2001 calibration) with weights equal to the reciprocal of the errors, yielding the value

$$d \log(O/H)/dR = -0.023 \pm 0.002 \text{ dex } \text{kpc}^{-1} \quad (7)$$

that we adopt as the slope of the oxygen abundance gradient in M31.

6 COMPARISON WITH OTHER METALLICITY INDICATORS

We have compared the H II region abundance gradient with the results obtained from young, BA-type supergiants and from planetary nebulae, which trace an older stellar population. Despite the relatively small distance to the Andromeda galaxy and the importance of this extragalactic neighbour in the context of galactic evolution studies, the analysis of a sizeable sample of blue supergiant spectra for the determination of stellar metallicities is still lacking. The situation has remained virtually unchanged during the past decade, since the publication of stellar metallicities for 7 B-type supergiants by Trundle et al. (2002), and, somewhat paradoxically, lags behind the quantitative spectroscopic study of massive stars in considerably more distant galaxies (e.g. Kudritzki et al. 2008, 2012). One of these stars had been originally analyzed by Smartt et al. (2001). Additionally, two A- and one F-type supergiants were investigated by Venn et al. (2000). More recently Przybilla, Butler, & Kudritzki (2006) revisited the metallicity derived for one of the A-type stars with more accurate non-LTE calculations, and analyzed a new A-type star. It should be pointed out that the B-type metallicities obtained by Trundle et al. (2002) were based on an LTE analysis, except for one case, in which the non-LTE metallicities were found to be consistent, within the relatively large (between ~ 0.2 and 0.4 dex) errors, even though they are 0.07 dex lower in the case of oxygen (a similar result is obtained comparing the LTE vs. non-LTE analysis of the star in common with Smartt et al. 2001).

These studies highlighted the difficulty of comparing the stellar and the nebular metallicities, due to the systematic differences in H II region abundances obtained from different strong-line methods. For this reason, the results of the comparison were inconclusive. Our new study of H II regions in M31 was mostly motivated by the need to acquire *direct* T_e -based nebular abundance. As this paper shows, we have partially succeeded in our goal, but the detection of auroral lines in H II region spectra remains elusive for M31 even with 10m-class telescopes.

In Fig. 9 we include the O/H abundances derived for the B-type supergiant stars by Trundle et al. (2002, yellow star symbols) and Smartt et al. (2001, red star symbol), and for the AF stars studied by Venn et al. (2000, green star symbols) and Przybilla et al. (2006, pink star symbols). When available, only the non-LTE result is shown. Galactocentric distances have been recalculated from our adopted M31 parameters (see Table 2). The comparison is somewhat complicated by the large errors in the B supergiant abundances, but it is obvious that a systematic offset is present in relation to the *direct* abundances we determined from H II regions. If we focus on the A-type supergiants (galactocentric distance ~ 11.7 kpc), which have more accurate abundances, the nebular O/H ratio lies ~ 0.3 dex below the stellar value. On the other hand, among the gradients obtained from strong-line diagnostics, we find that the N2 method, as calibrated by Pettini & Pagel (2004), is in acceptable agreement with the absolute value provided by the stars (the difference relative to the stars is reduced to ~ 0.1 dex). This situation contrasts the results obtained by our group in other, lower metallicity galaxies, for example NGC 300, where excellent agree-

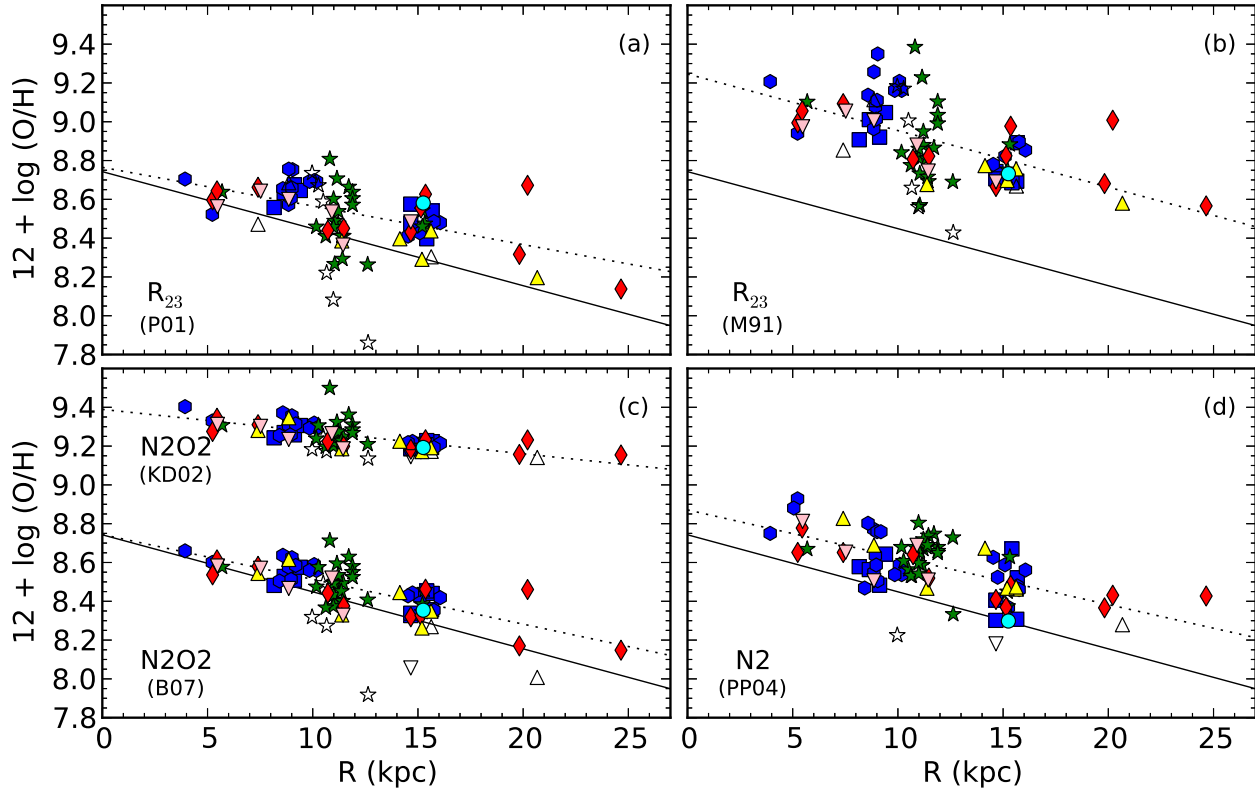


Figure 11. Same as Fig. 10, but for the H II regions analyzed in this paper plus H II regions spectroscopically observed by other authors: Dennefeld & Kunth (1981), yellow triangles; Blair et al. (1982), red diamonds; H II regions classified as ‘center–bright’ by Galarza et al. (1999), green stars; Bresolin et al. (1999), pink inverted triangles; region K932 (cyan circle) observed by Esteban et al. (2009), and H II regions analyzed in this paper (blue squares and hexagons, as in Fig. 10). Open symbols indicate H II regions with uncertain values in the relevant line ratios for a given empirical calibration, as stated by the corresponding authors. The dotted straight lines show the best linear fit to the oxygen abundance gradient obtained from the strong–line methods applied to the whole H II region dataset (excluding regions with uncertain line ratios). The solid straight line shows the oxygen abundance gradient obtained from the T_c –based method (Eq. 5).

Table 11. Linear least–squares fit parameters to the oxygen abundance distribution across the M31 disk obtained from different strong–line methods (see Sect. 5.1) applied to our H II region sample and to the whole set of spectroscopic data on M31 H II regions published so far: this paper, Dennefeld & Kunth (1981), Blair et al. (1982), Galarza et al. (1999), Bresolin et al. (1999), Esteban et al. (2009).

Method	slope (dex kpc ⁻¹)	zero point (dex)	Correlation coefficient	No. data points	Scatter ^a (dex)
Our H II region sample					
R ₂₃ (P01)	-0.021 ± 0.004	8.82 ± 0.05	-0.69	25	0.08
R ₂₃ (PT05)	-0.007 ± 0.007	8.45 ± 0.08	-0.20	25	0.12
R ₂₃ (M91)	-0.037 ± 0.008	9.39 ± 0.09	-0.70	25	0.14
N2O2 (B07)	-0.024 ± 0.003	8.77 ± 0.03	-0.86	28	0.05
N2O2 (KD02)	-0.015 ± 0.002	9.43 ± 0.02	-0.84	28	0.03
N2 (PP04)	-0.027 ± 0.006	8.88 ± 0.07	-0.65	31	0.12
H II regions from all authors					
R ₂₃ (P01)	-0.020 ± 0.004	8.76 ± 0.05	-0.55	70	0.12
R ₂₃ (PT05)	-0.009 ± 0.005	8.45 ± 0.06	-0.24	70	0.15
R ₂₃ (M91)	-0.029 ± 0.005	9.25 ± 0.06	-0.59	70	0.15
N2O2 (B07)	-0.023 ± 0.002	8.74 ± 0.03	-0.75	75	0.08
N2O2 (KD02)	-0.011 ± 0.002	9.39 ± 0.02	-0.66	75	0.05
N2 (PP04)	-0.024 ± 0.003	8.87 ± 0.04	-0.64	82	0.11

^a *rms* residual scatter, estimated as the square root of the arithmetic mean value of the squares of the difference between fitted and measured data.

ment is found between the metallicities obtained for stars and H II regions using *both* the direct T_e -based method and N2 (Bresolin et al. 2009a). A situation similar to what we encounter in M31 is also found for M81 (Patterson et al. 2012; Kudritzki et al. 2012). A possible interpretation of this discrepancies will be provided in the next section.

Recently Kwitter et al. (2012) published the abundance analysis of 16 PNe from [O III] λ 4363 detections in the outer disk ($R > 20$ kpc) of M31. The radial distribution of the O/H ratio is included in Fig. 9 (open circles; we recalculated the galactocentric distances from our adopted orientation parameters, Table 2, finding only minor differences). We note a striking offset between H II regions and PNe direct abundances (although we note that their target 16 falls near the H II region locus). It is not clear whether the two samples of objects are directly comparable, however, due to the fact that the PNe belong to the outer disk of the galaxy. Difficulties in the interpretation of the offset might also arise from the complicated chemical history of M31 (e.g. Davidge et al. 2012 for a recent summary). Finally, we note that the slope of the PNe O/H gradient obtained by Kwitter et al. (2012), -0.011 ± 0.004 dex kpc $^{-1}$, is somewhat flatter than the one we derive from H II regions. We add that a flatter gradient for PNe compared to H II regions has also been recently determined in the galaxy NGC 300 (Stasinska et al. 2012, in preparation), and corroborates recent model predictions of galactic chemical evolution (Pilkington et al. 2012).

7 DISCUSSION AND CONCLUSIONS

One of the main conclusions obtained in this paper is that the slope of the oxygen abundance gradient in M31 from the analysis of the H II regions is quite robust, approximately -0.023 dex kpc $^{-1}$, regardless of the choice of abundance diagnostic used (with the notable exception of the Pilyugin & Thuan 2005 and Kewley & Dopita 2002 calibrations). However, the ~ 0.3 dex offset between the *direct* abundances (obtained from the auroral line detections) and the stellar abundances is somewhat disturbing, especially considering the fact that the direct abundances also lie significantly below those obtained from strong-line methods that, by construction, should be in agreement with the direct determinations. Since the discrepancy could be a result of the higher metallicity of M31 compared to other galaxies where such offset is not observed, we suggest an interpretation based on biases affecting the direct abundances. As is well known, with increasing O/H the detection of the auroral lines in the spectra of H II regions becomes increasingly difficult. This is due to the exponential dependence of the line emissivities on the electron temperature, and the decreasing nebular temperatures with increasing metallicity due to more efficient cooling. As a result, very few auroral line detections exist in the literature for extragalactic H II regions with metallicity above solar. Therefore, given the metallicity (around the solar value) found for the supergiant stars in M31 it is not surprising that we only have a few [O III] λ 4363 detections. Under these conditions we would preferentially detect this line just for some of the hottest (less metal enriched) H II regions, which leads to a bias in the derived average oxygen abundance: the abundance estimated from the few [O III] λ 4363 detections would underestimate the mean

O/H ratio. This would explain why the auroral line-based abundances lie below the strong line abundances obtained from methods such as N2 and N2O2, which have been calibrated using H II regions with detections of auroral lines. If we assume an observational abundance scatter of ~ 0.07 dex (comparable to what has been measured in other nearby galaxies, see Bresolin et al. 2009a, Kennicutt et al. 2003, Bresolin 2011), we can expect to systematically underestimate the oxygen abundance by as much as ~ 0.15 dex if we assume that our auroral line detections refer to the hottest nebulae only, i.e. are not representative of the mean H II region population. Most of the remaining discrepancy with the stellar abundances could be explained by depletion of oxygen onto dust grains, which has been estimated to be ~ 0.12 dex at high metallicity (e.g. Mesa-Delgado et al. 2009, Peimbert & Peimbert 2010). If we account for these effects, the central abundance of M31 would be approximately $12 + \log(\text{O}/\text{H}) = 8.94 \pm 0.10$ dex; i.e. between 1.4 and 2.2 times the solar value.

Finally, we also point out that a discrepancy between *direct* nebular abundances and stellar abundances increasing with metallicity would naturally result from the presence of inhomogeneities in the temperature distribution within an H II region (Peimbert et al. 2007) or by the effect recently reported by Nicholls, Dopita, & Sutherland (2012), who proposed that the energy distribution of electrons in H II regions deviates from a Maxwell-Boltzmann one. Further tests of the mechanisms proposed here to explain the systematic offset between T_e -based H II region abundances and stellar metallicities would require to increase the sample of H II regions with *direct* abundance determinations for metal-rich (super-solar) galaxies, together with a program aimed at measuring metallicities of blue supergiant stars. In the specific case of M31, in particular, more accurate stellar abundance data for a large sample of B-type stars would be highly desirable.

ACKNOWLEDGMENTS

We kindly acknowledge Carrie Trundle for her contribution in the initial phases of this project. We also thank the anonymous referee for an encouraging report and constructive comments. A. Zurita acknowledges support from the Spanish ‘‘Plan Nacional del Espacio de Ministerio de Educaci3n y Ciencia’’ (via grant C-CONSOLIDER AYA 2007-67625-C02-02) and from the ‘‘Junta Andaluc3a’’ local government through the FQM-108 project and through the ‘‘ayudas individuales’’ program. F. Bresolin gratefully acknowledges the support from the National Science Foundation grants AST-0707911 and AST-1008798. A. Zurita would like to thank the Institute for Astronomy at Manoa, Honolulu for hospitality. F. Bresolin is grateful for the kind hospitality received at the Departamento de F3sica Te3rica y del Cosmos in Granada.

REFERENCES

- Allain D., Collin-Souffrin S., Joly M., Vigroux L., 1979, A&A, 78, 200
- Asplund M., Grevesse N., Sauval A. J., Scott P., 2009, ARA&A, 47, 481

- Baade W., Arp H., 1964, *ApJ*, 139, 1027
- Béland S., Boulade O., Davidge T., 1988, *BCFHT*, 19, 16
- Benjamin R. A., Skillman E. D., Smits D. P., 1999, *ApJ*, 514, 307
- Bernard E. J., et al., 2012, *MNRAS*, 420, 2625
- Blair W. P., Kirshner R. P., Chevalier R. A., 1982, *ApJ*, 254, 50
- Block D. L., et al., 2006, *Natur*, 443, 832
- Bohlin R. C., Colina L., Finley D. S., 1995, *AJ*, 110, 1316
- Bresolin F., Kennicutt R. C., Jr., Garnett D. R., 1999, *ApJ*, 510, 104
- Bresolin F., Garnett D. R., Kennicutt R. C., Jr., 2004, *ApJ*, 615, 228
- Bresolin F., Schaerer D., González Delgado R. M., Stasińska G., 2005, *A&A*, 441, 981
- Bresolin F., 2007, *ApJ*, 656, 186
- Bresolin F., Gieren W., Kudritzki R.-P., Pietrzyński G., Urbaneja M. A., Carraro G., 2009a, *ApJ*, 700, 309
- Bresolin F., Ryan-Weber Eg., Kennicutt R. C., Goddard Q., 2009b, *ApJ*, 695, 580
- Bresolin F., Stasińska G., Vílchez J. M., Simon J. D., Rosolowsky E., 2010, *MNRAS*, 404, 1679
- Bresolin F., 2011, *ApJ*, 730, 129
- Corbelli E., Lorenzoni S., Walterbos R., Braun R., Thilker D., 2010, *A&A*, 511, A89
- Davidge T. J., McConnachie A. W., Fardal M. A., Fliri J., Valls-Gabaud D., Chapman S. C., Lewis G. F., Rich R. M., 2012, *ApJ*, 751, 74
- Dennefeld M., Kunth D., 1981, *AJ*, 86, 989
- De Robertis M. M., Dufour R. J., Hunt R. W., 1987, *JRASC*, 81, 195
- de Vaucouleurs G., de Vaucouleurs A., Corwin H. G., Jr., Buta R. J., Paturel G., Fouque P., 1991, *trcb.book*,
- Dopita M. A., Evans I. N., 1986, *ApJ*, 307, 431
- Edmunds M. G., Pagel B. E. J., 1984, *MNRAS*, 211, 507
- Edmunds M. G., 1989, In *Evolutionary Phenomena in Galaxies*, p. 356, eds. Beckman, J. E. & Pagel B. E. J., Cambridge Univ. Press, Cambridge
- Esteban C., Bresolin F., Peimbert M., García-Rojas J., Peimbert A., Mesa-Delgado A., 2009, *ApJ*, 700, 654
- Ferguson A. M. N., Irwin M. J., Ibata R. A., Lewis G. F., Tanvir N. R., 2002, *AJ*, 124, 1452
- Ferguson A. M. N., Johnson R. A., Faria D. C., Irwin M. J., Ibata R. A., Johnston K. V., Lewis G. F., Tanvir N. R., 2005, *ApJ*, 622, L109
- Fesen R. A., Blair W. P., Kirshner R. P., 1985, *ApJ*, 292, 29
- French H. B., 1981, *ApJ*, 246, 434
- Galarza V. C., Walterbos R. A. M., Braun R., 1999, *AJ*, 118, 2775
- Garnett D. R., 1992, *AJ*, 103, 1330
- González-Delgado R. M., Cerviño M., Martins L. P., Leitherer C., Hauschildt P. H., 2005, *MNRAS*, 357, 945
- Hammer F., Puech M., Chemin L., Flores H., Lehnert M. D., 2007, *ApJ*, 662,
- Hamuy M., Suntzeff N. B., Heathcote S. R., Walker A. R., Gigoux P., Phillips M. M., 1994, *PASP*, 106, 566
- Howarth I. D., 1983, *MNRAS*, 203, 301
- Ibata R., Irwin M., Lewis G., Ferguson A. M. N., Tanvir N., 2001, *Natur*, 412, 49
- Izotov Y. I., Stasińska G., Meynet G., Guseva N. G., Thuan T. X., 2006, *A&A*, 448, 955
- Kennicutt R. C., Jr., Bresolin F., Garnett D. R., 2003, *ApJ*, 591, 801
- Kewley L. J., Dopita M. A., 2002, *ApJS*, 142, 35
- Kewley L. J., Ellison S. L., 2008, *ApJ*, 681, 1183
- Kudritzki R.-P., Urbaneja M. A., Bresolin F., Przybilla N., Gieren W., Pietrzyński G., 2008, *ApJ*, 681, 269
- Kudritzki R.-P., Urbaneja M. A., Gazak Z., Bresolin F., Przybilla N., Gieren W., Pietrzyński G., 2012, *ApJ*, 747, 15
- Kuzio de Naray R., McGaugh S. S., de Blok W. J. G., 2004, *MNRAS*, 355, 887
- Kwitter K. B., Lehman E. M. M., Balick B., Henry R. B. C., 2012, *ApJ*, 753, 12
- Liu X.-W., Storey P. J., Barlow M. J., Danziger I. J., Cohen M., Bryce M., 2000, *MNRAS*, 312, 585
- Lodders K., 2003, *ApJ*, 591, 1220
- López-Sánchez Á. R., Esteban C., 2010, *A&A*, 517, A85
- Magrini L., et al., 2002, *A&A*, 386, 869
- Mallery R. P., et al., 2007, *ApJS*, 173,
- Marcon-Uchida M. M., Matteucci F., Costa R. D. D., 2010, *A&A*, 520, A35
- McCall M. L., Rybski P. M., Shields G. A., 1985, *ApJS*, 57, 1
- McGaugh S. S., 1991, *ApJ*, 380, 140
- Mesa-Delgado A., Esteban C., García-Rojas J., Luridiana V., Bautista M., Rodríguez M., López-Martín L., Peimbert M., 2009, *MNRAS*, 395, 855
- Monet D. G., 1998, *AAS*, 30, #120.03
- Nicholls D. C., Dopita, M. A., Sutherland, R. S., 2012, *ApJ*, 752, 148
- Oke J. B., 1990, *AJ*, 99, 1621
- Oke J. B., Cohen, J. G., Carr, M., Cromer, J., Dingizian A., Harris F. H., Labrecque S., Lucinio R., Schaal W., Epps H., Miller J., 1995, *PASP*, 107, 375
- Pagel B. E. J., Edmunds M. G., Blackwell D. E., Chun M. S., Smith G., 1979, *MNRAS*, 189, 95
- Pagel B. E. J., Edmunds M. G., Smith G., 1980, *MNRAS*, 193, 219
- Patterson M. T., Walterbos R. A. M., Kennicutt R. C., Chiappini C., Thilker D. A., 2012, *MNRAS*, 422, 401
- Peimbert M., Costero R., 1969, *BOTT*, 5, 3
- Peimbert M., Peimbert A., Esteban C., García-Rojas J., Bresolin F., Carigi L., Ruiz M. T., López-Sánchez A. R., 2007, *RMxAC*, 29, 72
- Peimbert A., Peimbert M., 2010, *ApJ*, 724, 791
- Pellet A., Astier N., Viale A., Courtes G., Maucherat A., Monnet G., Simien F., 1978, *A&AS*, 31, 439
- Pérez-Montero E., Díaz A. I., 2003, *MNRAS*, 346, 105
- Pérez-Montero E., Díaz A. I., 2005, *MNRAS*, 361, 1063
- Pettini M., Pagel B. E. J., 2004, *MNRAS*, 348, L59
- Pilkington K. et al., 2012, *A&A*, 540, 56
- Pilyugin L. S., 2001, *A&A*, 369, 594
- Pilyugin L. S., Thuan T. X., 2005, *ApJ*, 631, 231
- Porter R. L., Ferland G. J., MacAdam K. B., 2007, *ApJ*, 657, 327
- Przybilla N., Butler K., Kudritzki R.-P., 2006, *astro*, arXiv:astro-ph/0611044
- Renda A., Kawata D., Fenner Y., Gibson B. K., 2005, *MNRAS*, 356, 1071, 322
- Ribas I., Jordi C., Vilardell F., Fitzpatrick E. L., Hilditch R. W., Guinan E. F., 2005, *ApJ*, 635, L37
- Rubin V. C., Krishna Kumar C., Ford W. K., Jr., 1972,

- ApJ, 177, 31
- Sabbadin F., Minello S., Bianchini A., 1977, A&A, 60, 147
- Seaton M. J., 1979, MNRAS, 187, 73P
- Shaw R. A., Dufour R. J., 1995, PASP, 107, 896
- Skillman E. D., 1989, ApJ, 347, 883
- Skrutskie M. F., et al., 2006, AJ, 131, 1163
- Smartt S. J., Crowther P. A., Dufton P. L., Lennon D. J., Kudritzki R. P., Herrero A., McCarthy J. K., Bresolin F., 2001, MNRAS, 325, 257
- Stasińska G., 1978, A&A, 66, 257
- Stasińska G., Schaerer D., Leitherer C., 2001, A&A, 370, 1
- Storey P. J., Hummer D. G., 1995, MNRAS, 272, 41
- Stupar M., Parker Q. A., Filipović M. D., 2008, MNRAS, 390, 1037
- Tanaka M., Chiba M., Komiyama Y., Guhathakurta P., Kalirai J. S., Iye M., 2010, ApJ, 708, 1168
- Trundle C., Dufton P. L., Lennon D. J., Smartt S. J., Urbaneja M. A., 2002, A&A, 395, 519
- Unwin S. C., 1983, MNRAS, 205, 773
- van Dokkum P. G., 2001, PASP, 113, 1420
- Venn K. A., McCarthy J. K., Lennon D. J., Przybilla N., Kudritzki R. P., Lemke M., 2000, ApJ, 541, 610
- Vila-Costas M. B., Edmunds M. G., 1992, MNRAS, 259, 121
- Vila Costas M. B., Edmunds M. G., 1993, MNRAS, 265, 199 482
- Vilardell F., Ribas I., Jordi C., Fitzpatrick E. L., Guinan E. F., 2010, A&A, 509, A70
- Vílchez J. M., Pagel B. E. J., 1988, MNRAS, 231, 257
- Williams B. F., 2003, AJ, 126, 1312
- Yin J., Hou J. L., Prantzos N., Boissier S., Chang R. X., Shen S. Y., Zhang B., 2009, A&A, 505, 497
- Zaritsky D., Kennicutt R. C., Jr., Huchra J. P., 1994, ApJ, 420, 87